Measurement report: Hygroscopicity of Size-Selected Aerosol Particles in the Heavily Polluted Urban Atmosphere of Delhi: Impacts of Chloride Aerosol

Anil Kumar Mandariya[1,2], Ajit Ahlawat[3], Mohammed Haneef[1], Nisar Ali Baig[1], Kanan Patel[4], Joshua Apte[5], Lea Hildebrandt Ruiz[4], Alfred Wiedensohler[3]*, and Gazala Habib[1]*

[1]Department of Civil Engineering, Indian Institute of Technology Delhi, New Delhi, India

[2]now at: Univ Paris Est Creteil and University Paris Cité, CNRS, LISA, F – 94010 Créteil, France

[3]Leibniz Institute for Tropospheric Research (TROPOS), Permoserstraße, 15 Leipzig, Germany

[4]Department of Civil, Architectural and Environmental Engineering, The University of Texas at Austin, Austin, Texas, USA

[5]McKetta Department of Chemical Engineering, The University of Texas at Austin, Austin, Texas, USA

Correspondence to: Gazala Habib (gazalahabib@civil.iitd.ac.in) and Alfred Wiedensohler (ali@tropos.de)

Abstract. Recent research has revealed the crucial role of winter-time, episodic high chloride (H-Cl) emissions in the Delhi region, which significantly impact aerosol hygroscopicity and aerosol-bound liquid water, thus contributing to the initiation of Delhi fog episodes. However, these findings have primarily relied on modeled aerosol hygroscopicity, necessitating validation through direct hygroscopicity measurements. This study presents the measurements of non-refractory bulk aerosol composition of PM_1 from an Aerodyne aerosol chemical speciation monitor and for first-time size-resolved hygroscopic growth factors (Nucleation, Aitken, and Accumulated mode particles) along with their associated hygroscopicity parameters at 90% relative humidity using a hygroscopic-tandem differential mobility analyzer at the Delhi Aerosol Supersite. Our observations demonstrate that the hygroscopicity parameter for aerosol particles varies from 0.00 to 0.11 (with an average of 0.03 ± 0.02) for 20 nm particles, 0.05 to 0.22 (0.11 ± 0.03) for 50 nm particles, 0.05 to 0.30 (0.14 ± 0.04) for 100 nm particles, 0.05 to 0.41 (0.18 ± 0.06) for 150 nm particles, and 0.05 to 0.56 (0.22 ± 0.07) for 200 nm particles. Surprisingly, our findings demonstrate that the period with H-Cl emissions displays notably greater hygroscopicity (0.35 ± 0.06) in comparison to spans marked by high biomass burning (0.18 ± 0.04), high hydrocarbon-like organic aerosol (0.17 ± 0.05), and relatively cleaner periods (0.27 ± 0.07). This research presents initial observational proof that ammonium chloride is the main factor behind aerosol hygroscopic growth and aerosol-bound liquid water content in Delhi. The finding emphasizes, ammonium chloride's role in aerosol-water interaction and related haze/fog development. Moreover, the high chloride levels in aerosols seem to prevent the adverse impact of high organic aerosol concentrations on cloud condensation nuclei activity.

1. Introduction

The Intergovernmental Panel on Climate Change (IPCC) (Intergovernmental Panel on Climate Change, 2023) reported that the interaction between aerosols and clouds is not completely comprehended, and there are significant uncertainties in gauging global radiative budgets. In order to overcome and elucidate these uncertainties, the role of aerosol hygroscopicity is crucial. Hygroscopicity is a critical factor in comprehendling how aerosol particles functions as cloud condensation nuclei (CCN) and create fog droplets/haze under sub-saturated/nearly saturation conditions, as well as forming cloud droplets at atmospheric supersaturation levels (McFiggans et al., 2006; Topping and McFiggans, 2012). Its comprehension is vital to better predicting the aerosol size distribution and scattering properties with more accuracy in global models under varying atmospheric humidity (RH) conditions (Randall et al., 2007). Hygroscopicity at higher RH results in an increase in the cross-sectional area of the aerosol, leading to efficient light scattering by the aerosol particles (Tang and Munkelwitz, 1994). This phenomenon is primarily dependent on the chemical composition and particle size. Generally, ammonium salts of sulfate, nitrate, and chloride, which are inorganic salts, exhibit high hygroscopicity (Hu et al., 2011; Petters and Kreidenweis, 2007). In contrast, organic aerosols (OAs) have relatively lower hygroscopicity (Jimenez et al., 2009; Kroll et al., 2011), and dust particles and black/elemental carbon particles are known to be hydrophobic (Seinfeld and Pandis, 2006). The increased atmospheric humidity during winter and monsoon seasons promotes the development of more oxidized secondary organic aerosol (SOA) through aqueous-phase (Ervens et al., 2011) and heterogeneous reactions (McNeill, 2015). This process leads to a heightened organic aerosol hygroscopicity (Jimenez et al., 2009; Mei et al., 2013), which negatively impacts the local visibility (Li et al., 2016; Liu et al., 2012). Conversely, aerosol loading has an inverse effect on aerosol hygroscopicity (Mandariya et al., 2020a). In addition, aerosol loading plays a critical role in determining cloud lifetime, which impacts the amount of rainfall in the region (Albrecht, 1989; Lohmann and Feichter, 2005).

Over the past few decades, researchers have extensively measured aerosol hygroscopicity using a hygroscopic tandem differential mobility analyzer (H-TDMA) (Massling et al., 2005; Gysel et al., 2007; Mandariya et al., 2020; Swietlicki et al., 2008; Yeung et al., 2014; Kecorius et al., 2019) and a CCN counter (Bhattu and Tripathi, 2015; Gunthe et al., 2011; Massoli et al., 2010; Ogawa et al., 2016) under sub- and supersaturated conditions, respectively. Petters and Kreidenweis (2007) introduced the hygroscopicity parameter, kappa (κ), to correlate aerosol hygroscopicity with its chemical composition. Hygroscopicity of OA may differ according to their chemical properties such as solubility, extent of dissociation in aerosol water, and surface activity, which can pose

challenges in quantifying OA hygroscopicity (Hallquist et al., 2009; Jimenez et al., 2009). As a result, this introduces further discrepancies in predicted and measured aerosol hygroscopicity. Therefore, there is a requirement to investigate the measurement-based aerosol hygroscopicity of Delhi's atmosphere to gain a better understanding of the recurring occurrences of haze and cloud formations.

In recent decades, rapid economic growth and industrialization in the Indo-Gangetic Plain (IGP) have resulted in significantly poor air quality during the winter season (Wester et al., 2019). Local and regional air pollution issues may potentially affect Delhi during this time (Arub et al., 2020; Bhandari et al., 2020; Gani et al., 2019; Prakash et al., 2018). Recent studies have indicated that chloride significantly contributes to the degradation of air quality in the Delhi region and favors haze/fog formation during winter (Gunthe et al., 2021). Gani et al. (2019) and Rai et al. (2020) support these findings. Trash and biomass burning for heating and waste degradation have been identified as major sources of chloride in Delhi (Rai et al., 2020). A recent study conducted in Delhi revealed that frequent high chloride events promote high levels of aerosol liquid water content under elevated humid conditions. This leads to haze and poor visibility in the city (Chen et al., 2022). Additionally, Gunthe et al. (2021) found that higher chloride levels also enhance aerosol hygroscopicity. However, it is important to note that this particular study was based on theoretical hygroscopicity. Therefore, it is crucial to study the effects of chloride on aerosol hygroscopicity and its ability to increase the amount of aerosol-bound liquid water based on field measurements. In addition, the heavily polluted urban atmosphere, with its highly complex composition, severely limits the hygroscopicity of the aerosol particles. This is particularly evident in cities like Delhi, located in the IGP of India, where air quality deteriorates significantly during haze/fog-dominated periods. To the author's best knowledge, this study is the first to explore the complex atmosphere of IGP in Delhi, India, using aerosol hygroscopicity measured by H-TDMA.
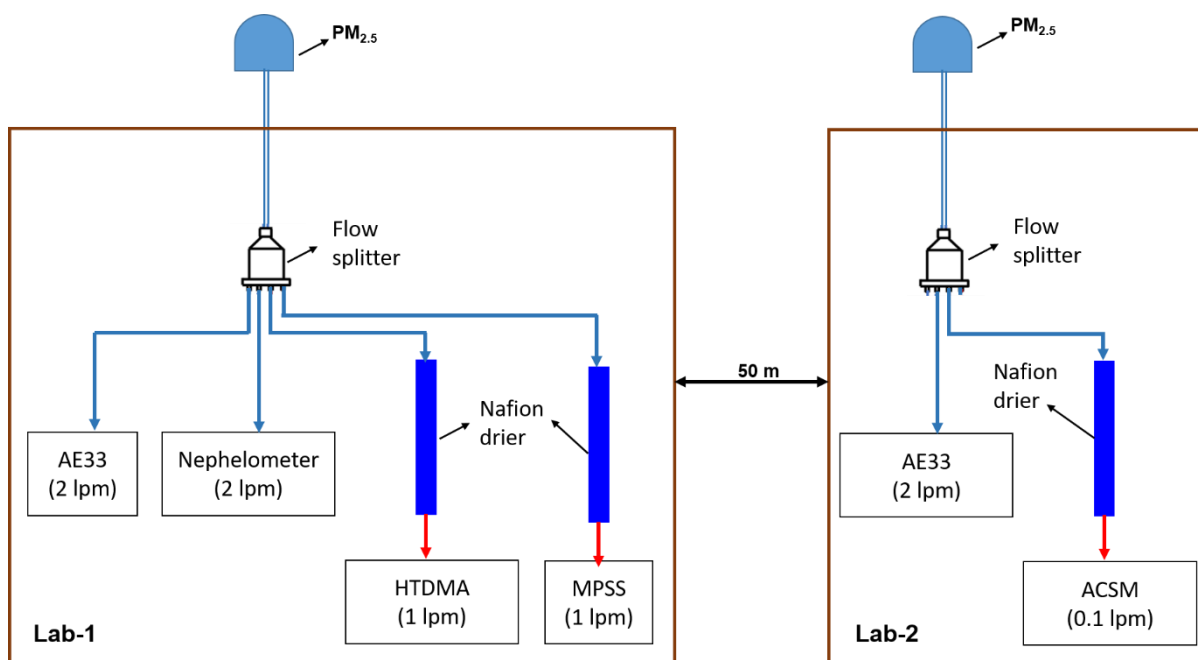
2. Experimental Methods

2.1 Aerosol Measurements

Real-time measurements of atmospheric aerosols were conducted during winter (February 1, 2020 to March 20, 2020) at Indian Institute of Technology (IIT) Delhi, Block 5. H-TDMA, TROPOS-type Mobility Particle Size Spectrometer (MPSS), and Aerodyne Aerosol Chemical Speciation Monitor (ACSM) from Aerodyne Research in Billerica, MA were used simultaneously at a height of approximately 15 meters above ground level (a.g.l.) as depicted in Fig. 1. Lab-2 is located 50 meters away from Lab-1. The ACSM is utilized to quantify mass

90   concentrations of organic aerosol (OA), ammonium (NH$_4$), sulfate (SO$_4$), nitrate (NO$_3$), and chloride (Cl) in non-

91   refractory particulate matter less than 1 μm (NR-PM$_1$).

92   The hygroscopic growth of size-resolved particles at 90 % RH was investigated using the HTDMA system in this

93   study. The HTDMA system has been utilized in numerous field campaigns before (Massling et al., 2007; Wu et

94   al., 2013b; Zhang et al., 2016). The HTDMA system (TROPOS, Germany) consists of two Differential Mobility

95   Analyzers (DMAs) of the Hauke-median type (TROPOS, Germany), along with a Condensation Particle Counter

96   (CPC) Model 3772 by TSI Inc. (USA), and a humidifier system situated between the two DMAs. The initial

97   DMA's function is to choose quasi-monodisperse particles at a dry diameter (D$_p$, dry) of 30% RH. Technical

98   abbreviations will be explicated at their first usage. After passing through a humidity conditioner, the humidity of

99   the size-selected particles can be adjusted from 30% to 90% RH by mixing dry air with RH<5% and moist air

100   with ~95% RH via regulating aerosol and sheath air flow (Maßling et al., 2003). The associated uncertainties with

101   RH measurement at 90% RH are 1.0%. The particle hygroscopic growth distribution at a specific humidity and

102   dry size (D$_p$, dry) can be conveniently determined through CPC. There are two humidity sensors (Vaisala) in the

103   system for aerosol flow and sheath flow respectively. The sensors in the second DMA were calibrated

104   automatically every 30 min at 90% RH using 100 nm ammonium sulfate ((NH$_4$)$_2$SO$_4$) particles to analyze stability

105   at high RH. The measurement error of the HTDMA depends mainly on RH measurement and control uncertainties

106   within the system (Su et al., 2010). All RH sensors were calibrated using the Vaisala salt kit containing LiCl,

107   NaCl, KCl and so forth, before the measurement campaign. Size calibration for both DMAs involved the

108   application of Latex particles of standard size, 200 nm prior to measurement. The number concentration peak

109   occurred at 203 nm, which attests to the accuracy of DMAs' size selection at 1.5%. The HTDMA system was

110   used to measure the hygroscopic growth factors (HGFs) of particles with D$_p$, dry of five different sizes (20, 50,

111   100, 150 and 200 nm), at 90% RH. The full scan covering all five sizes had a time resolution of approximately 30

112   minutes.

113   Particle number size distributions (PNSDs) and particle volume-size distributions (PVSDs) were measured using

114   a MPSS.

115

PM$_{2.5}$

Flow splitter

Nafion drier

AE33 (2 lpm)   Nephelometer (2 lpm)

HTDMA (1 lpm)   MPSS (1 lpm)

Lab-1

50 m

PM$_{2.5}$

Flow splitter

Nafion drier

AE33 (2 lpm)

ACSM (0.1 lpm)

Lab-2

Figure 1: Schematic diagram of the inlet systems for aerosol sampling instruments. The blue and red sampling lines indicate the ambient air and dehumidified (RH<25%) ambient air, respectively.

2.2 Meteorological and Gas Data

The gas data was obtained from the R.K. Puram-DPCC monitoring station, a continuous ambient air quality monitoring station managed by the central control room for air quality management (Delhi-NCR). The data was downloaded from the CPCB website (https://app.cpcbccr.com/ccr/#/caaqm-dashboard/caaqm-landing/data). R.K. Puram is situated 3.5 km northwest of IIT Delhi. The automatic weather station (Watch Dog 2000 series) continuously measured wind speed (WS), wind direction (WD), temperature (T), and relative humidity (RH). The station is installed on the rooftop of the 9th-floor building at IITD.

2.3 Data Analysis

2.3.1 H-TDMA

Overall, we conducted 1483 cycles of HTDMA scans. After each cycle, we calculated the percentage difference between the measured and theoretical growth factors (Δq) for 100 nm ammonium sulfate particles. Only those cycles with $\Delta q \leq \pm 5\%$ were included for further data analysis, while the remaining cycles were discarded (Kecorius et al., 2019). As a result, we obtained 1102 HTDMA scan cycles that passed this data quality check. Regarding good scan cycles, we conducted 1449, 1431, 1438, 1470, and 1420 successful H-TDMA scans for particles of sizes 20, 50, 100, 150, and 200 nm particles, respectively, for further analysis. Subsequently, we

5

applied TDMAinv Toolkit, a piecewise linear TDMAinv algorithm developed by Gysel et al. (2009) and written in IgorPro, to perform post-data processing on the raw HGF data. The measured distribution function is a smoothed and skewed integral transformation of actual probability density functions for growth factors (GF-PDFs). Gysel et al. (2009) provides a detailed account of the raw data processing in the TDMAinv toolkit for the measurement of real HGFs. The TDMAinv toolkit was successfully employed in various studies across the globe (Gysel et al., 2007; Liu et al., 2012; Sjogren et al., 2007; Wang et al., 2018a), including Kanpur, India (Mandariya et al., 2020a). Furthermore, the RH in DMA2 generally reached the designated 90% value and remained stable within ±1%. However, on occasion, it experienced significant drifts. To address this issue, all growth factors measured between 88% and 92% RH were adjusted to the target value of 90% (HGF_90%) (Gysel et al., 2007) with the kappa-model recommended in the TDMAinv toolkit (Gysel et al., 2009). This approach effectively minimized the RH drifts in DMA2. After conducting scans at target RH for aerosol particles of 20, 50, 100, 150, and 200 nm, 979, 957, 972, 969, and 966 of these scans were respectively corrected. The corrected scans were then averaged for a 60-minute time resolution, resulting in 425, 429, 419, 424, and 417 scans.

Furthermore, using the kappa-Köhler theory (Mandariya et al., 2020a; Petters and Kreidenweis, 2007), we calculated the size-resolved hygroscopicity factors (kappa, κ, say $\kappa_{\text{H-TDMA\_90\%}}$) from the corresponding size-resolved target RH corrected HGFs, based on equation (1).

$$\kappa_{H-TDMA\_90\%} = (HGF\_90\%^3 - 1)\left[\frac{1}{RH}\,exp\left(\frac{4\sigma M_w}{RT\rho_w D_o HGF_{90}\%}\right) - 1\right], \qquad (1)$$

Where, $\kappa_{\text{H-TDMA\_90\%}}$ represents the hygroscopicity factor at 90% RH, while HGF_90% is the size-resolve HGF at 90% RH. RH stands for atmospheric relative humidity expressed as a fraction, and σ denotes the surface tension of the aerosol liquid droplet-air interface at the droplet surface measured in N/m, assumed to be nearly to pure water. R represents the universal gas constant, expressed in units of J K^{-1} mol^{-1}. M_w denotes the molecular mass of water while T signifies the ambient temperature in Kelvin (K). ρ_w signifies the density of water in kg/m^3. D_o denotes the dry mobility diameter of the particle in meters (m).

2.3.2 MPSS

The electrical mobility distribution is measured by MPSS and then converted to PNSD in the 8 to approximately 800 nm mobility diameter range. This is achieved by utilizing an inversion algorithm to correct for multiple charged aerosol particles (Wiedensohler, 1988; Pfieffer et al., 2014) and diffusional losses (Wiedensohler et al., 2012; 2018).

2.3.3 ACSM

For a detailed account of the ACSM setup, please refer to Arub et al. (2020). The ACSM operated in a temperature-controlled laboratory at almost 0.1 lpm and 1-minute time resolution. It was set to measure mass-to-charge ratio (m/z) from 10 to 140. The PM$_1$ aerosol beam was concentrated and directed towards the vaporizer at 600 °C. The flash-vaporized compounds were then ionized through impact ionization at 70 eV electrons and detected using a quadrupole mass spectrometer (Ng et al., 2011). The study employed a 200 millisecond amu^{-1} scan speed and a pause setting of 125 for a sampling duration of 64 seconds to collect aerosol mass spectra using the ACSM technique. Refer to Gani et al. (2019) for comprehensive guidance on the ACSM operational procedures. For ACSM calibration and data processing, please refer to Patel et al. (2021). Positive matrix factorization (PMF) was conducted on the data, resulting in a four-factor solution: hydrocarbon-like OA (HOA), biomass burning OA (BBO), less-oxidized OA (LO-OOA), and more-oxidized OA (MO-OOA), as shown in Fig. S1. More information regarding PMF analysis can be found in section S.1 and Fig. S2 of the Supplementary information. Three different events were identified based on the temporal variation of mass concentration peaks of BBOA, HOA, and Cl (see Fig. 2): 1) a high-residential or biomass burning period (H-BB); 2) a high-hydrocarbon-like OA period (H-HOA); and 3) a high-chloride period (H-Cl). Additionally, the "Clean Period" was defined as a period where the PM$_1$ loading was less than the 25th percentiles (≤ 38.7 µg m^{-3}) for the sampling period. The event's starting and ending times were determined by the initial increase in concentration and subsequent return to the starting values as the concentration decreased.

2.3.4 Derived Secondary Inorganic Salts

The ACSM measures OA, NO$_3$, SO$_4$, NH$_4$, and Cl. A simplified ion-pairing scheme from Gysel et al. (2007) was adopted. However, NH$_4$Cl was not included in their ion-pairing scheme; therefore, we modified it to integrate ammonium chloride into the calculation. Thus, our modified ion-pairing scheme includes NH$_4$Cl (ACl), NH$_4$NO$_3$ (AN), (NH$_4$)$_2$SO$_4$ (AS), NH$_4$HSO$_4$ (ABS), and H$_2$SO$_4$ (SA) as shown below:

Case-1 $R_{SO_4}(NH_4 \ to \ SO_4) \leq 1$

$$SA = 98.0795 \times \max\left(0, (n_S - n_A)\right)$$

$$ABS = 115.11 \times n_A$$

$$AS = 0$$

189 $AN = 0$

190 $ACl = 0$

191 **Case-2 $1 < R_{SO_4} < 2$**

192 $SA = 0$

193 $ABS = 115.11 \times \left((2 \times n_S) - n_A\right)$

194 $AS = 132.1405 \times (n_S - n_A)$

195 $AN = 0$

196 $ACl = 0$

197 **Case-3 $R_{SO_4} \geq 2$**

198 $SA = 0$

199 $ABS = 0$

200 $AS = 132.1405 \times n_S$

201 $$AN = \left(\min\left(\left(n_A - \left(\frac{ABS}{115.11}\right) - \left(\frac{(2 \times AS)}{132.1405}\right)\right), n_N\right)\right) \times 80.0434$$

202 $$ACl = \left(\min\left(n_C, \left(n_A - \left(\frac{ABS}{115.11}\right) - \left(\frac{2 \times AS}{132.1405}\right) - \left(\frac{AN}{80.0434}\right)\right)\right)\right) \times 53.54$$

203 Here, "n" represents the number of moles, while "A", "N", "S", and "C" represents the species NH_4, NO_3, SO_4,

204 and Cl. Inorganic salts concentrations were also predicted using the NH_4, SO_4, NO_3, and Cl components of the

205 ISORROPIA v2.1 model. Our results show a strong correlation and nearly unit slope (0.9999) between the

206 calculated and modeled inorganic salts, as presented in Fig. S3. This strongly justifies the new ion-pairing scheme

207 utilized in this study.

208

2.3.5 Windrose and Potential Source Contribution Function (PSCF)

The windrose plot was generated using the openair package in R (http://www.r-project.org, http://www.openair-project.org). An offline based Hybrid Single-Particle Lagrangian Integrated Trajectory (HYSPLIT4) model developed by NOAA/Air Resources Laboratory (ARL)) (Draxler and Hess, 1997) was used to estimate the 48-hour back trajectory of air masses that reached DSL at 500 m above ground for the entire study period at hourly intervals.. The meteorological data used for back trajectories was obtained from ARL's Global Data Assimilation System archive, specifically the GDAS 0.5 degree archive (http://ready.arl. noaa.gov/archives.php). We used these estimated back trajectories and the measured mass fraction of chemical species of bulk aerosol as input in conducting Potential Source Contribution Function (PSCF) analysis. This analysis was carried out with the aid of Zefir (version 3.7), a tool written in Igor Pro (WaveMetrics). The Zefir tool is described in detail elsewhere (Petit et al., 2017). Additionally, this tool was used to create the box plots discussed in the following section. To calculate the aerosol liquid water content (ALWC) as a function of inorganic species mass concentration, ambient T, and RH, the ISORROPIA-II model (Fountoukis and Nenes, 2007) was utilized.

3. Result and Discussions

3.1 Overview of meteorology, trace gases, and aerosol characterization

Fig. 2 depicts the hourly-resolved temporal changes of various meteorological parameters, including RH, T, WD, and WS, PNSD, PVSD, principal components of non-refractory PM_1, and OA with their corresponding fractional mass contributions. In addition, Fig. S4 exhibits the temporal fluctuations of atmospheric gases, specifically nitrogen oxides (NOx), carbon monoxide (CO), and sulfur dioxide (SO_2). Delhi's winter climate is mainly affected by a depression caused by Western Disturbances, resulting in cold waves in the region. The ambient RH and T vary within the range of 24.2% to 96.6% and 9.0 °C to 28.5 °C, respectively. The average values of RH and T are 56.0% ± 18.2% and 18.7 °C ± 4.2 °C, respectively. These fluctuations indicate a shift in Delhi's atmosphere transitions from being damp and chilly in February to dry and relatively warm in March. Nighttime conditions are consistently cooler and more humid than daytime conditions throughout the sampling period. Ambient RH exhibits a diurnal pattern, with a peak occurring during the early morning hours (06:00-07:00) and a valley appearing around midday (13:00-15:00). Conversely, ambient temperature follows an opposing trend, increasing at midday, which can be correlated with higher solar radiation during those hours (refer to Fig. 3a & b). The high ambient temperature and peak O_3 concentration observed during midday (see Fig. 3(i)) indicate the possibility of daytime photo-oxidation processes according to research carried out by Nelson et al. (2023). Fig. S5 displays the

238   variation of WS and WD, ranging from 0.0 to 5.6 (with an average of 1.0 ± 1.0) m/s and 4.0 to 345.7 (with an

239   average of 197.1 ± 84.4) degrees from the North, respectively. The majority of wind directions were in the WNW-

240   WSW and E-ESE direction. These patterns indicate that the air quality in Delhi remained relatively stagnant

241   throughout the study period. The measured aerosols are likely to be a result of local emissions and aerosol
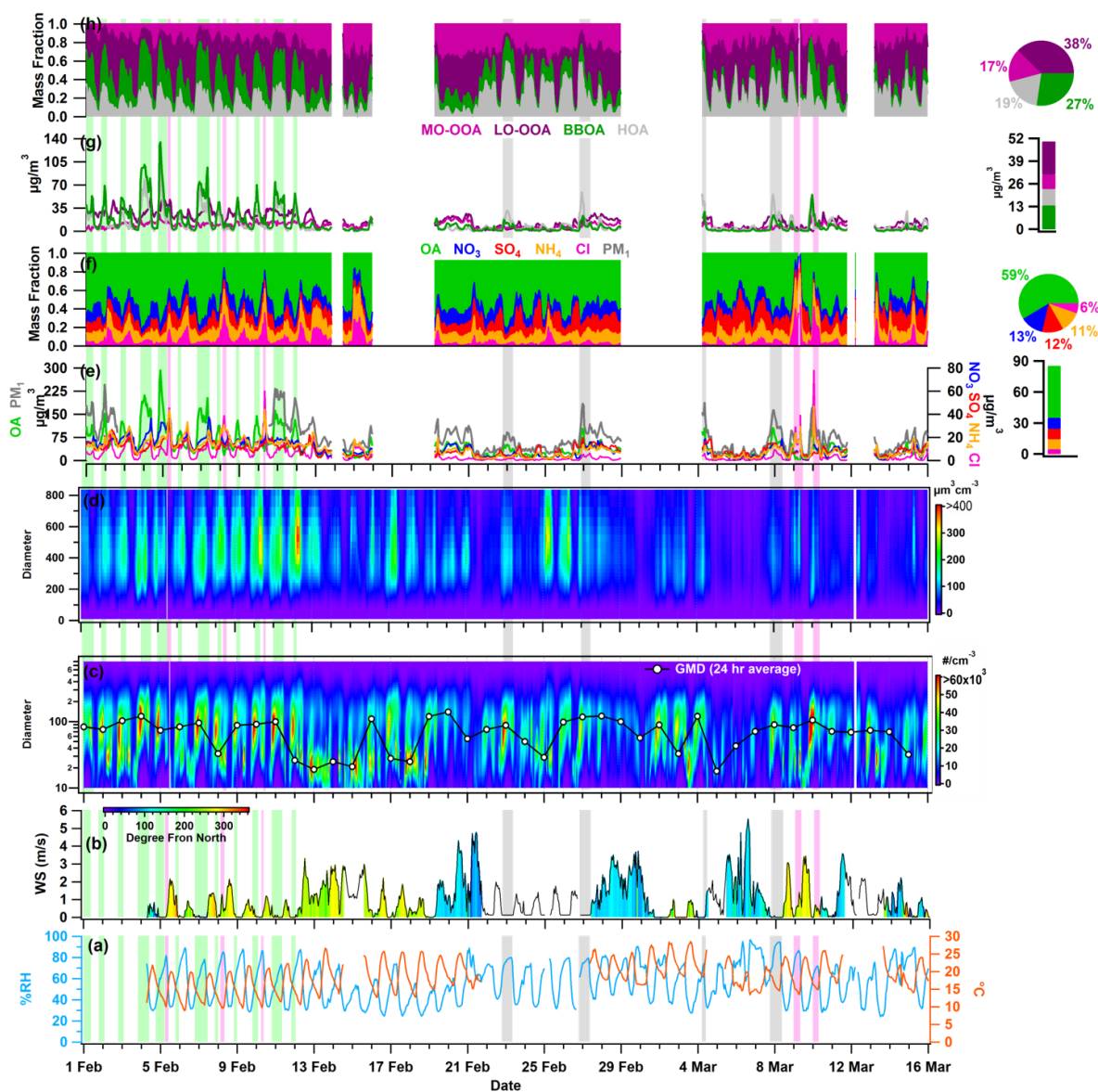
242   chemistry.

243   Throughout the sampling period, ambient trace gases NOx and CO demonstrate notable variability, peaking from

244   local burning activities. During intense biomass burning activities, ambient NOx levels reach a maximum of 421.2

245   ppb (58.4 ± 61.9). CO concentrations also reach maximum levels during similar periods as NOx, varying from

246   0.0 to 7.66 ppm (0.58 ± 0.79), as illustrated in Fig. S4. The time-specific changes in the levels of these trace gases

247   are illustrated in Fig. 3 (f, g, h, and i). The graph indicates two crests (06:00-08:00 and 17:00-20:00 hours), which

248   are attributed to local biomass/trash burning emissions that happen in the morning and heavy traffic during

249   nighttime rush hours. Conversely, SO_2 demonstrates a distinct pattern, with varying concentrations ranging from

250   0.46 to 9.55 ppb (4.41 ± 1.20). Notably, it exhibits peaks during the morning (09:00-12:00 hours) and at midnight

251   (21:00-02:00 hours), which are connected to local industrial stack emissions.

252   The PM_1 particle number concentration ranges from 408 to 29,845 particles/cm^3 (11319 ± 5552). Elevated particle

253   number concentrations are commonly linked to local burning incidents. The particle concentration sees a rise in

254   the evening (at 06:00 PM) and peaks at midnight, implying an increase in residential burning activity and traffic

255   exhaust emissions. These activities likely contribute to the decrease in the geometric mean diameter (GMD) of

256   the PNSD, which is around 47 nm. However, this value increases to nearly 87 nm, as shown in Fig. 3(t), indicating

257   the organic aerosol's nighttime aging. Fig. 3(y) depicts that the hourly averaged mean diurnal GMD of PVSD

258   varies from about 274 to 324 nm, with a mean value of 309.1 ± 33.1 nm. This average is similar to the higher-end

259   particle size of 200 nm hygroscopicity measurement used in this study. Therefore, the ACSM bulk aerosol

260   composition is the most appropriate option for discussing the hygroscopicity of these particles.

261   The PM_1 concentration, also known as hourly time-resolved NR-PM_1, ranged from 9.0 to 357.9 μg/m^3 with an

262   average of 81.2 ± 56.6 μg/m^3. This range is consistent with the 12.7-392 μg/m^3 (NR-PM_1) boundary previously

263   reported by Gani et al. (2019) at the same sampling location. Prakash et al. (2018) found that PM_1 mass

264   concentration accounts for 83% of $PM_{2.5}$, indicating the prevalence of combustion-based particles. Additionally,

265   we observed a high correlation (r^2 = 0.83, p<0.05) between PM_1 measured by ACSM and MPSS, assuming an

266   effective aerosol density of 1.6 g/cm^3 (refer to Fig. S6). The OA ranged from 1 and 293 (46.5 ± 39.6) μg/m^3, with

267 PM$_1$ being the predominant fraction. These findings are consistent with the range of 53.3 to 166 (112) μg/m^3

268 observed during the winter months (December-February) at the same location (Gani et al., 2019). However, the

269 decrease in average OA concentration during the measuring period of February-March can be explained by the

270 reduction in aerosol loading after its peak in December-January (Gupta and Mandariya, 2013). The campaign

271 average fractional contribution of OA to PM$_1$ was 56%, with a range of 1 to 84%. This high OA concentration in

272 fine particulate matter (PM$_1$) aligns with findings from prior studies in the IGP, including those conducted by

273 Chakraborty et al. (2016a), Gani et al. (2019), and Mandariya et al. (2019), as well as those conducted worldwide,

274 such as by Jimenez et al. (2009) and Zhang et al. (2007). Peak OA mass concentrations were observed between

275 9:00 PM and 11:00 PM (figure 2(k)), which is in line with observations made at the same site by Gani et al. (2019)

276 and Rai et al. (2020). The average mass concentration of NO$_3$ during the campaign was 10.1 ± 7.0 μg/m^3,

277 exhibiting diurnal variation with distinct peaks in the morning and at midnight (Fig. 3(l)). Additionally, SO$_4$

278 demonstrated a slight enhancement at 08:00 hr, and its concentration remained relatively stable from noon to

279 17:00 hr (Fig. 3(m)). Conversely, Cl experienced significant fluctuations, ranging from 0.13 to 77.83 μg/m^3, with

280 higher concentrations of Cl occurring episodically throughout the campaign. The Cl concentration aligns with

281 Gani et al. (2019)'s previously reported value of 0.1-66.6 μg/m^3 at the same location. Fig. 2(g and h) illustrates

282 the temporal variation of various OA factors. The mass concentration of BBOA peaks during the nighttime and

283 morning hours (Fig. 3(r)). On the other hand, LO-OOA exhibits a peak in the morning and remains relatively

284 stable at noontime, indicating a steady formation. Meanwhile, MO-OOA exhibited a slight rise around midday,

285 suggesting daytime photooxidation formation (Mandariya et al., 2019; Sun et al., 2016). During the sampling

286 period, oxygenated organic aerosol (OOA) comprised the majority of OA. The BBOA mass concentration during

287 H-BB events varied dynamically, ranging from 16.3 to 134.7 μg/m^3, with an average of 50.7 ± 24.0 μg/m^3.

288 Concurrently, these events displayed higher levels of HOA, ranging from 9.6 to 109.4 μg/m^3, indicating a likely

289 similarity in the sources of HOA during this particular incident. However, during H-HOA events, concentration

290 of HOA were higher, ranging from 4.8 to 58.9 μg/m^3, although these amounts were notably lower than those

291 observed during H-BB events. Nonetheless, the fractional mass contribution of HOA to OA was the largest of all

292 OA categories. Additionally, during H-Cl events, there were increased concentrations of both primary organic

293 aerosol HOA and BBOA. BBOA made up about 40.0%, 21.1%, 32.5%, and 13.1% to OA during H-BB, H-HOA,

294 H-Cl, and relatively clean events, respectively, indicating varied sources of BBOA. Furthermore, the average

295 contribution of H-HOA was the highest during the H-HOA event, at 41.6%. During the H-Cl event, Cl's
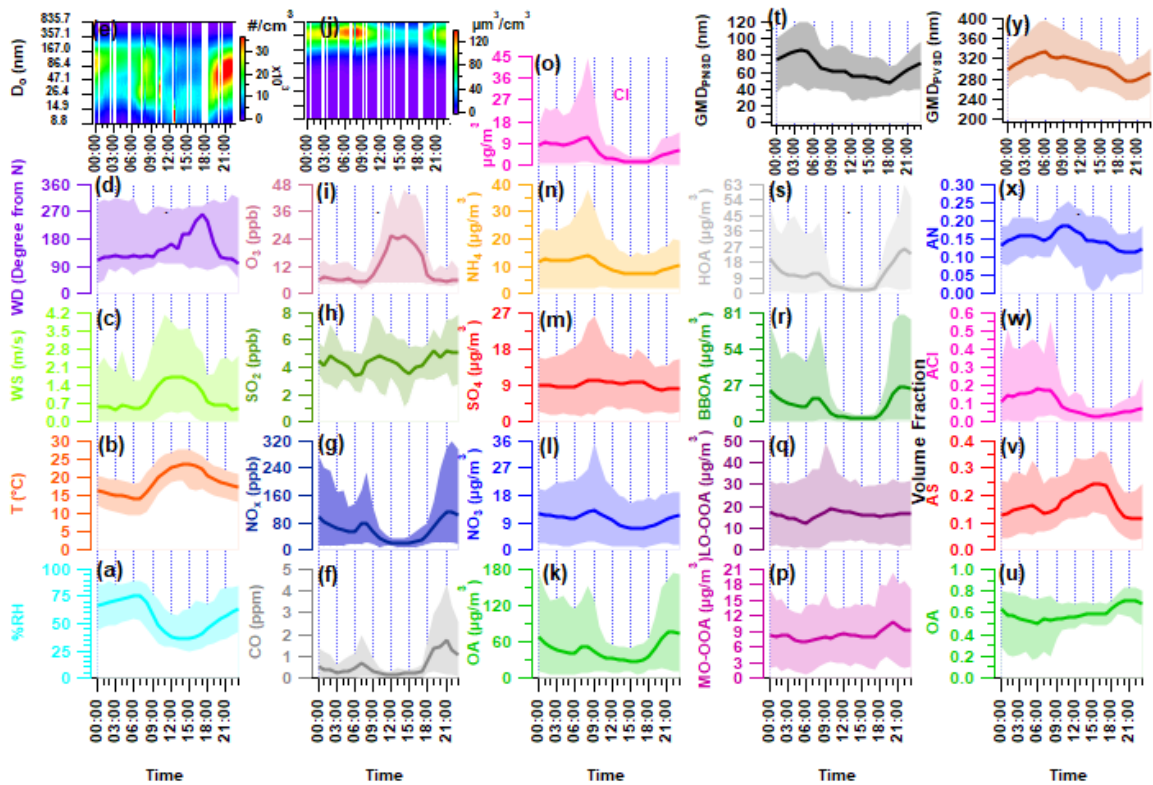
contribution to the fractional mass in PM$_1$ peaked up to 44.9%, which was higher than the contributions of 21.2% in H-BB events and 7.3% in H-HOA events.

Figure 2: Temporal variability of ambient (a) relative humidity (RH), temperature (T), (b) wind speed (WS), wind direction (WD), (c) particle number-size distribution (PNSD), 24-average geometric mean diameter (GMD), (d) particle volume-size distribution (PVSD), (e) particulate matter (PM$_1$), organic aerosol (OA), nitrate (NO$_3$), sulfate (SO$_4$), ammonium (NH$_4$), chloride (Cl), (f) fractional contribution of OA, NO$_3$, SO$_4$, NH$_4$, and Cl in PM$_1$, (g) more oxidized-oxygenated OA (MO-OOA), less oxidized-oxygenated OA (LO-OOA), biomass burning OA (BBOA), hydrocarbon like-OA (HOA), and (h) fractional contribution of MO-OOA, LO-OOA, BBOA, and HOA in OA. The pie chart sub-plot represents the overall average contribution of species, and the bar sub-plot represents the overall campaign average value of different species. All other species are represented with specific color coding mentioned in legends. The light

Figure 3: Diurnal variation of ambient meteorological parameters (a) % ambient relative humidity (RH), (b) temperature (T), (c) wind speed (WS), (d) wind direction (WD), and (e) particle number size distribution (PNSD), mass concentration of ambient trace gases (f) carbon mono-oxide (CO), (g) nitrogen oxides (NOx), (h) sulfur dioxide (SO$_2$), and (i) ozone (O$_3$), (j) particle volume size distribution (PVSD), mass concentration of aerosol constituents (k) organic aerosol (OA), (l) nitrate (NO$_3$), (m) sulfate (SO$_4$), (n) ammonia (NH$_4$), and (o) chloride (Cl), mass concentration of organic aerosol species (p) more oxidized-oxygenated OA (MO-OOA), (q) less oxidized-oxygenated OA (LO-OOA), (r) biomass burning OA (BBOA), and (s) hydrocarbon like-OA (HOA), (t) geometric mean diameter of particle number size distribution (GMD$_{PNSD}$) and volume fractional contribution of (u) organic aerosol (OA), (v) ammonium sulfate (AS), (w) ammonium chloride (ACl), and (x) ammonium nitrate (AN) in PM$_1$, and (y) geometric mean diameter of particle volume size distribution (GMD$_{PVSD}$). Upper and lower boundary of shaded area represents the 95th and 5th percentile values of respective species.
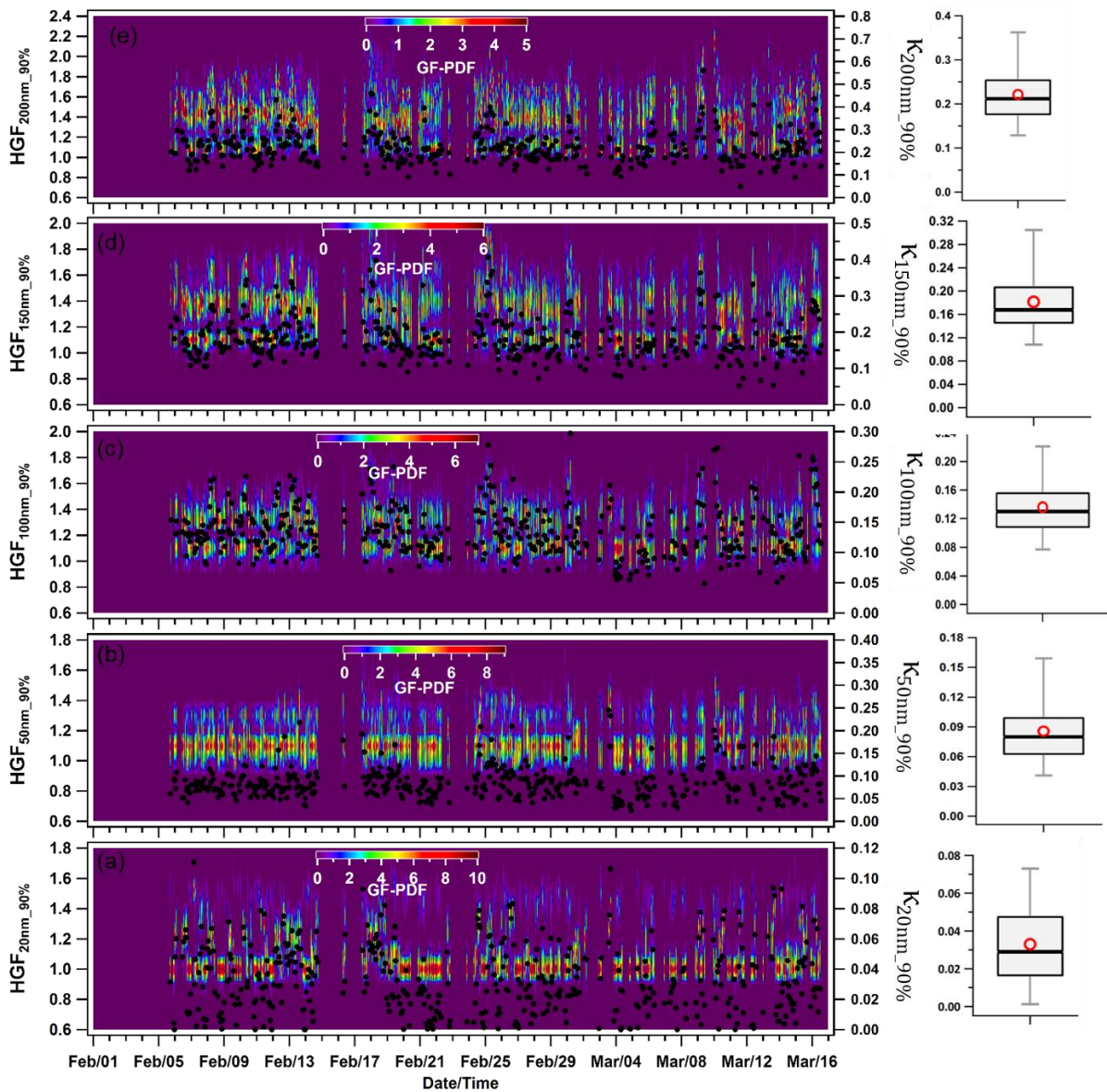
3.2 Hygroscopicity of Nucleation, Aitken, and Accumulation Mode Particles

3.2.1 Temporal variability

324 Fig. 4 displays the hourly averaged dynamic variability of $HGF_{90\%}$ and $\kappa_{H\text{-}TDMA\_90\%}$ (kappa) for aerosol particles

325 in the Nucleation, Aitken, and Accumulation modes at 90% ambient relative humidity. The hygroscopic growth

326 factors of particles sized at 20 ($HGF_{90\%\_20nm}$), 50 ($HGF_{90\%\_50nm}$), 100 ($HGF_{90\%\_100nm}$), 150 ($HGF_{90\%\_150nm}$), and 200

327 nm ($HGF_{90\%\_200nm}$) varied between 1.00-1.41, 1.05-1.39, 1.11-1.49, 1.12-1.63, and 1.12-1.79. The averaged

328 hygroscopic growth factors of the 20, 50, 100, 150, and 200 nm aerosol particles were 1.14 ± 0.09 (average ±

329 standard deviation), 1.16 ± 0.06, 1.27 ± 0.07, 1.35 ± 0.09, and 1.41 ± 0.09, respectively. These values indicate

330 statistical significance ($p<0.05$) between the different hygroscopic growth factors. Moreover, the hygroscopicity

331 values ($\kappa_{20nm\_90\%}$ and $\kappa_{50nm\_90\%}$) of the aerosol particles were found to range between 0.00-0.11 and 0.02-0.25 for

332 the 20 nm and 50 nm particle sizes, respectively, with an average of 0.03 ± 0.02 and 0.09 ± 0.03. Nucleation mode

333 particles, consisting mainly of monomodal GF-PDF (Fig. 4(a)), consisted of approximately 74 ± 24% nearly

334 hydrophobic particles (HGF <1.2). However, this percentage increased to 100% and was associated with nighttime

335 local burning activities, as demonstrated in Fig. 4(a). The nucleation mode particles ($\kappa_{20nm\_90\%}$) exhibited

336 significantly ($p<0.05$) lower hygroscopicity than the Aitken mode particles ($\kappa_{50nm\_90\%}$). Hong et al. (2015) found

337 that nucleation mode particles have higher susceptibility to condensable vapors such as newly-emitted VOCs,

338 H_2SO_4 and HCl. Nevertheless, the study at hand did not measure these substances. The κ value of Aitken-sized

339 particles was comparable to the 0.24 ± 0.08 of 52.6 ± 6.9 size particles reported by Gunthe et al. (2011) for Beijing,

340 like Delhi, is one of the most polluted urban area. Gunthe et al. (2011) conducted this study on CCN at

341 supersaturation levels, justifying the comparison. The campaign average hygroscopicity parameter (kappa, $\kappa_{90\%}$)

342 increased significantly ($p<0.05$) with particle size, attributed to the Kelvin effect (Wang et al., 2018a). In the

343 accumulation size range of 100, 150, and 200 nm, $\kappa_{90\%}$ increased to approximately 0.56. The mean values for

344 $\kappa_{100nm\_90\%}$, $\kappa_{150nm\_90\%}$, and $\kappa_{200nm\_90\%}$ were 0.14 ± 0.04, 0.18 ± 0.06, and 0.22 ± 0.07, respectively. The range for

345 $\kappa_{200nm\_90\%}$ was between 0.05 and 0.56. Similar variations of κ with particle size have been observed globally

346 (Cerully et al., 2015; Enroth et al., 2018; Fan et al., 2020; Kawana et al., 2016; Kim et al., 2020; Kitamori et al.,

347 2009; Ogawa et al., 2016; Sjogren et al., 2012; Wang et al., 2018a), including in Kanpur, India, situated in the

348 center of the IGP (Mandariya et al., 2020a). These variations have been attributed to the prevalent increase in

349 inorganic to organic aerosol fraction in particles with size increment. Furthermore, Arub et al. (2020) reported

350 that $\kappa_{H\text{-}TDMA\_90\%}$ was approximately in the range of 0.13-0.77 for PM_1 in Delhi, without considering BC. However,

351 their theoretical prediction of particles' hygroscopicity took into account a particle's chemical composition,

352 leading to more precise results. Arub et al. (2020) thus provided a theoretical prediction of particles'

353 hygroscopicity by considering a particle's chemical composition. A 10% in κ calculation was observed when

14

354 considering BC in the aerosol chemical composition. Additionally, the $\kappa_{\text{H-TDMA\_90\%}}$ measured in this study aligned

355 with the global average value of 0.27 ± 0.21 for continental aerosols (Petters and Kreidenweis, 2007; Pringle et

356 al., 2010). Subsequent sections will discuss the impact of a particle's chemical composition, local meteorology,

357 and air mass trajectories on $\kappa_{\text{H-TDMA\_90\%}}$ for accumulation mode particles.

358

359

360 **Figure 4: Temporal variability in hygroscopicity parameter kappa (κ) of nucleation mode particles (a) 20 nm**

361 **($\kappa_{20nm\_90\%}$), Aitken mode particles (b) 50 nm ($\kappa_{50nm\_90\%}$), and Accumulation mode particles (c) 100 nm ($\kappa_{100nm\_90\%}$), (d)**

362 **150 nm ($\kappa_{150nm\_90\%}$), and (e) 200 nm ($\kappa_{200nm\_90\%}$). The box plots represent the variability in the hygroscopicity of**

363 **respective sizes of particles in which low and high whisker traces represent the 5 and 95 percentile, respectively. The**
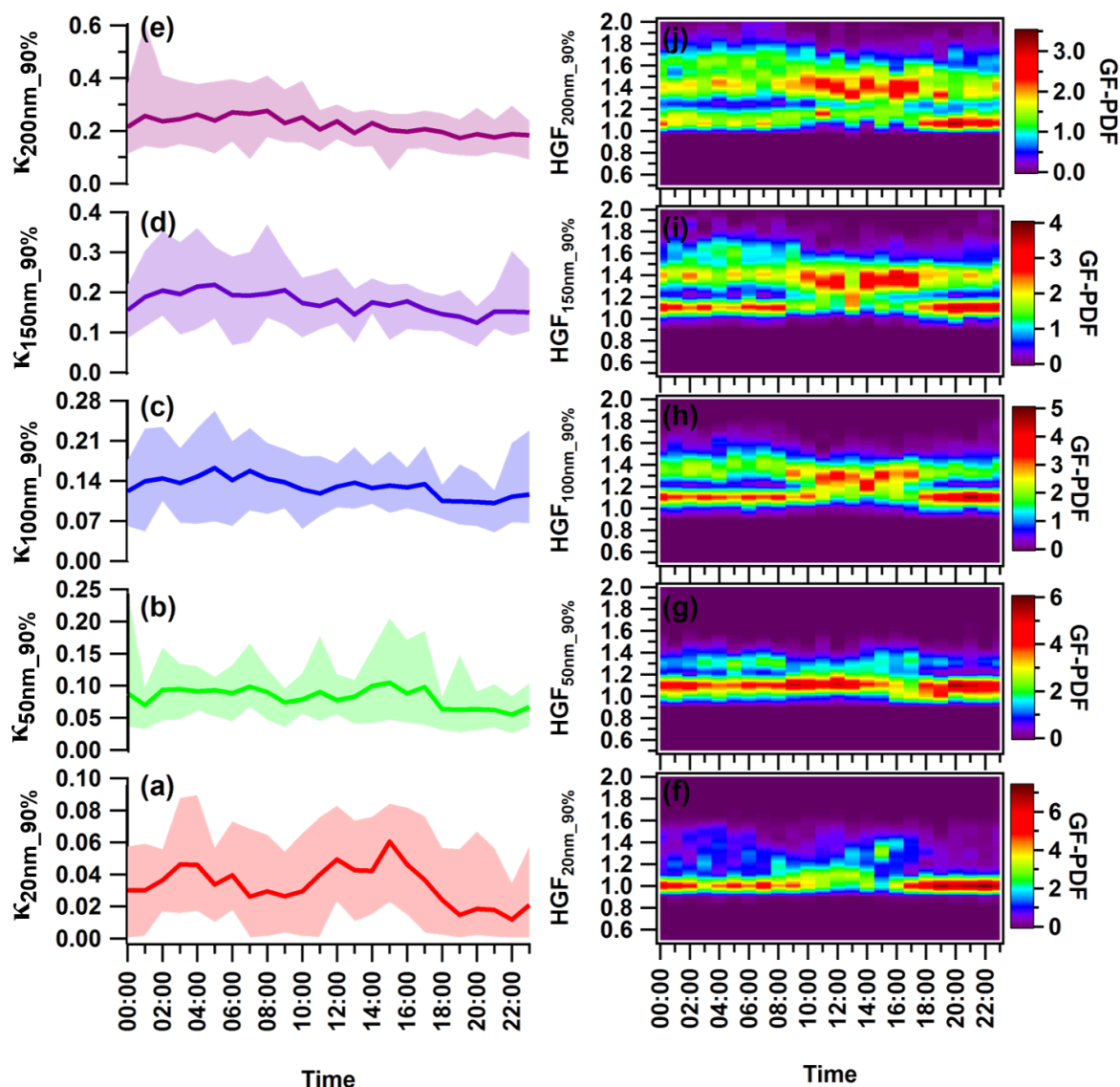
364 **red marker indicates the average of the data, whereas the upper and lower sides of the boxes indicate the 75 and 25**

365 **percentile of the data, respectively.**

366 **3.2.2 Diurnal variability**

367 The diurnal variation in $\kappa_{\text{H-TDMA\_90\%}}$ differed for nucleation ($\kappa_{\text{20nm\_90\%}}$), Aitken ($\kappa_{\text{50nm\_90\%}}$), and Accumulation

368 ($\kappa_{\text{100nm\_90\%}}$, $\kappa_{\text{150nm\_90\%}}$, and $\kappa_{\text{200nm\_90\%}}$) mode particles. Fig. 5 illustrates the hourly-resolved average κ for each

369 particle size, showing a diel trend. The larger particles displayed higher κ values than the smaller ones, consistent

370 with trends observed in Kanpur, India (Mandariya et al., 2020a) and other locations worldwide (Fan et al., 2020;

371 Hong et al., 2015). Overall, all particle sizes exhibited a "late-night hump" (02:00-05:00 hr) in $\kappa_{\text{H-TDMA\_90\%}}$. Only

372 $\kappa_{\text{20nm\_90\%}}$ displayed a diurnal variation with two peaks: one occurring late at night (02:00-04:00 hr) and the other

373 at noon (14:00-16:00 hr). Additionally, two valleys were observed during the morning (07:00-10:00 hr) and night

374 (19:00-22:00 hr), which indicate the strong influence of local burning and traffic activities (Pringle et al., 2010).

375 Furthermore, nucleation-sized particles were potentially contributed by nearly hydrophobic particles (HGF<1.2)

376 from evening to midnight. Mono-modal GF-PDF was exhibited around a unit hygroscopic growth factor,

377 potentially suggesting the presence of locally-emitted particles. The 20 nm particles are of sufficient small size to

378 be classified as nucleation mode particles. Similar diurnal trends of Nucleation and Aitken mode particles have

379 been observed by Achtert et al. (2009), who attributed the lower values to the emission of hydrophobic aerosol

380 particles during the local burning emissions. The daytime hump in aerosol particle composition can be attributed

381 to the intensity of the photochemical oxidation process, resulting in the amplification of more oxidized species.

382 Moreover, the gaseous condensation of H_2SO_4, HNO_3, and VOCs predominantly controls their chemical makeup

383 (Hong et al., 2015). The variability of $\kappa_{\text{H-TDMA\_90\%}}$ can be addressed by taking into account the chemical

384 composition of the aerosol. Although $\kappa_{\text{50nm\_90\%}}$ exhibited less variation, it follows a diurnal pattern similar to

385 $\kappa_{\text{20nm\_90\%}}$. Furthermore, when the dry size of the aerosol particles increased to the accumulated mode, the diurnal

386 variation shifted towards nearly constant for the rest of the day. Hong et al. (2018) found no discernible diurnal

387 variation of 100- and 150-nm particles of organic-dominated aerosols in China's Pearl River Delta region.

388 Furthermore, the diurnal cycles of aerosol physicochemical properties also reflect the dynamic diurnal variation

389 in the planetary boundary layer (PBL), leading to particle accumulation during the night. The study only addressed

390 trend variability using bulk-aerosol composition, as size-resolved chemical composition was not quantified.

391 However, the daily average aerosol PNSD ranged from 18.0-140.0 nm, with a mean of 73.1 ± 33.8 nm. The shift

392 in PVSD mode occurred in the 300-600 nm. Range, making it appropriate to analyze the $\kappa_{\text{200nm\_90\%}}$ variation in

16

393   association with the bulk chemical properties of aerosols. Fan et al. (2020) demonstrated in Fig. 3 (r, s t, u, and v)

394   that the increase in the ratio of inorganic volume fraction to OA volume fractions is responsible for the peak in

395   hygroscopicity observed in the early morning hours. Additionally, in the winter during mid-night and early

396   morning, water-soluble organic and inorganic gases undergo partitioning and/or coagulation/condensation on the

397   surface of pre-existing particles. Furthermore, at high RH and lower temperatures, primary and secondary, less-

398   oxidized organic aerosols engage in the aging process. This leads to improved oxidation through

399   aqueous/heterogeneous reactions, thereby increasing the hygroscopicity of the particles (Jimenez et al., 2009; Wu

400   et al., 2016). Similar findings were reported by Fan et al. (2020) for winter in urban Beijing. They have attributed

401   this to the increase in hygroscopic particles due to the aqueous-oxidation and/or condensation process on the pre-

402   existing particles. Generally, stronger noontime solar radiation promotes more intense photooxidation processes.

403   The process promotes the distribution of fairly more oxidized and less volatile organics on the surface of particles,

404   thus augmenting the hygroscopic nature of particles that belong to the accumulation mode (Duplissy et al., 2011;

405   Massoli et al., 2010; Tritscher et al., 2011). The $\kappa_{H\text{-}TDMA\_90\%}$ exhibited a noontime flattening pattern, which was

406   due to a combination of the positive and negative effects resulting from an increase in the volume fraction of OA

407   and more hygroscopic ammonium sulfate and a decrease in ACl, and AN's volume fraction. A potential factor

408   that modulates the hygroscopicity of accumulation mode particles is the lower volume fraction contribution of

409   highly volatile ACl. This correlation is strongly supported by the $\kappa_{H\text{-}TDMA\_90\%}$ and the volume fraction of ACl (ε_{ACl})
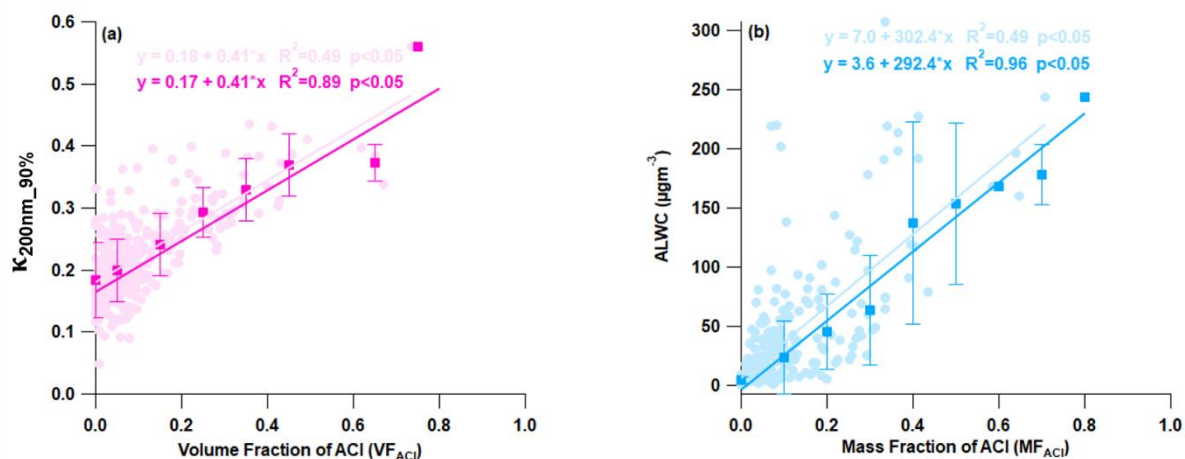
410   in the corresponding size particles.

Figure 5: Diurnal variance in the hygroscopic parameter kappa (κ) of nucleation mode particles (a) 20 nm ($\kappa_{20nm\_90\%}$), Aitken mode particles (b) 50 nm ($\kappa_{50nm\_90\%}$), and Accumulation mode particles (c) 100 nm ($\kappa_{100nm\_90\%}$), (d) 150 nm ($\kappa_{150nm\_90\%}$), and (e) 200 nm ($\kappa_{200nm\_90\%}$) and hygroscopic growth factor of (f) 20 nm (HGF$_{20nm\_90\%}$), (g) 50 nm (HGF$_{50nm\_90\%}$), (h) 100 nm (HGF$_{200nm\_90\%}$), (i) 150 nm (HGF$_{150nm\_90\%}$), and 200 nm ($\kappa_{200nm\_90\%}$) aerosol particles. The solid line represents diurnal average values, and the upper and lower shaded area represents 95 and 5 percentile values of corresponding average values. Different color coding has been used to represent various size-specific kappa values. The color scale represents the growth factor probability density function of hygroscopic growth factor.

3.2.3 Driving Factor of Hygroscopicity

A correlation analysis was conducted between the measured chemical species and aerosol hygroscopicity to investigate the factors governing aerosol hygroscopicity, as presented in Fig. 6. It was found that organic aerosol

18

422 negatively affected κ, as evidenced by a negative correlation (Fig. S7(a)). The negative correlation between OA

423 and κ has been noted in India (Bhattu et al., 2016; Mandariya et al., 2020b) and globally (Enroth et al., 2018;

424 Hong et al., 2014; Kawana et al., 2016; Kitamori et al., 2009; Wang et al., 2018a; Wu et al., 2013a). These findings

425 suggest that primary constituents were predominant during high loading and may have been nearly hydrophobic

426 or less hygroscopic. The present study found that a 10% increase in volume of OA in 200 nm aerosol particles led

427 to a 4% reduction in their ability to attract water (hygroscopicity) (Fig. S7(a)). It is noteworthy that ammonium

428 sulfate and nitrate exhibited a weak positive correlation with hygroscopicity (Fig. 7(b and c)). This may be

429 attributed to sulfate and nitrate aerosols dominant in larger particles (>200nm). However, increasing the volume

430 of AN and AS by 10% resulted in a 3.2 and 1.6% increase in hygroscopicity, respctively. This demonstrates that

431 even small changes can have a significant impact on the final product, highlighting the importance of careful

432 consideration and attention to detail. If the aerosol composition had an increased AN and AS contribution, the

433 water-bound capacity of the aerosol was positively and negatively affected, respectively (refer to Fig. S8).

434 Additionally, as shown in Fig. 6(a), there was an increase in the volume fraction of ACl in PM_1 with an increase

435 in aerosol hygroscopicity. This strong positive correlation was responsible for a 4.2% increase in kappa over the

436 increment of 10% ACl by volume. This was the highest among all chemical species. Furthermore, ammonium

437 chloride has a greater capacity for water absorption (Chen et al., 2022; Zhao et al., 2020), which is supported by

438 the strong correlation between ALWC and the mass fraction of ACl in PM_1 as demonstrated in Fig. 6(b). The

439 increasing fraction of ACl in PM_1 may therefore be attributed to the higher water uptake potential of ammonium

440 chloride. This implies that particles with a higher proportion of ammonium chloride absorb more water vapor,

441 resulting in larger hygroscopic aerosol particles. It is evident that the rise in ammonium chloride proportion

442 amplifies aerosol liquid water content, resulting in greater aerosol particle hygroscopicity. A recent study

443 conducted in Delhi by Chen et al. (2022) revealed that the fraction of ammonium chloride in PM_1 aerosol increases

444 significantly during higher relative humidity conditions in the winter season. This is due to the co-condensation

445 of semivolatile ammonium chloride with water vapor on particles, leading to enhanced water uptake and severe

446 winter haze in Delhi. The high volume fractions (over 30%) of ACl in atmospheric PM_1 were observed

447 sporadically, leading to the conclusion that the high chloride fraction in the particle phase heavily relies on excess

448 ammonia in the atmosphere. These findings suggest that ammonia plays a crucial role in determining chloride

449 partitioning in the particle phase, leading to increased aerosol water content in high relative humidity conditions

450 and lower temperature. The concentration of ACl relies heavily on both RH and temperature.

(a)

$y = 0.18 + 0.41^*x \quad R^2=0.49 \quad p<0.05$

$y = 0.17 + 0.41^*x \quad R^2=0.89 \quad p<0.05$

$\kappa_{200nm\_90\%}$

Volume Fraction of ACl (VF$_{ACl}$)

(b)

$y = 7.0 + 302.4^*x \quad R^2=0.49 \quad p<0.05$

$y = 3.6 + 292.4^*x \quad R^2=0.96 \quad p<0.05$

ALWC (μgm^{-3})

Mass Fraction of ACl (MF$_{ACl}$)

Figure 6: Correlation plot for (a) κ$_{200nm\_90\%}$ vs volume fraction of ammonium chloride aerosol (VF$_{ACl}$) and (b) aerosol liquid water content (ALWC) vs mass fraction of ammonium chloride (MF$_{ACl}$). The solid circle and square marker represent the individual data points and the average of 10% volume and mass fraction increment of ACl data points, respectively. The light and dark color regression lines and equations indicate the overall and average (10% volume and mass fraction increment) correlation, respectively. The error bars indicate the standard deviation of the data points within the 10% mass and volume fractional bins.

3.2.4 Hygroscopicity during high biomass burning (H-BB), high-hydrocarbon like OA (H-HOA), high-Cl (H-Cl), and relatively clean periods

Delhi's atmosphere is a complex mixture of chloride and organic aerosol sources resulting from combustion (including crop residue, agriculture waste, medical waste, municipal waste, plastic, etc.) and industrial activity. To examine the influence of chloride and OA on aerosol hygroscopicity, all episodic events were categorized into three groups. The first group was H-BB events, the second group was H-HOA events, and the third group was H-Cl events. Aerosol chemical composition data was filtered based on hygroscopic parameter data for subsequent analysis. This facilitates the retrieval of data specific to local emissions and atmospheric chemistry, as well as the effects of various potential transported air masses. Extracting any conceivable information pertaining to aerosol sources and transformation processes is valuable in interpreting their impact on aerosol hygroscopicity.
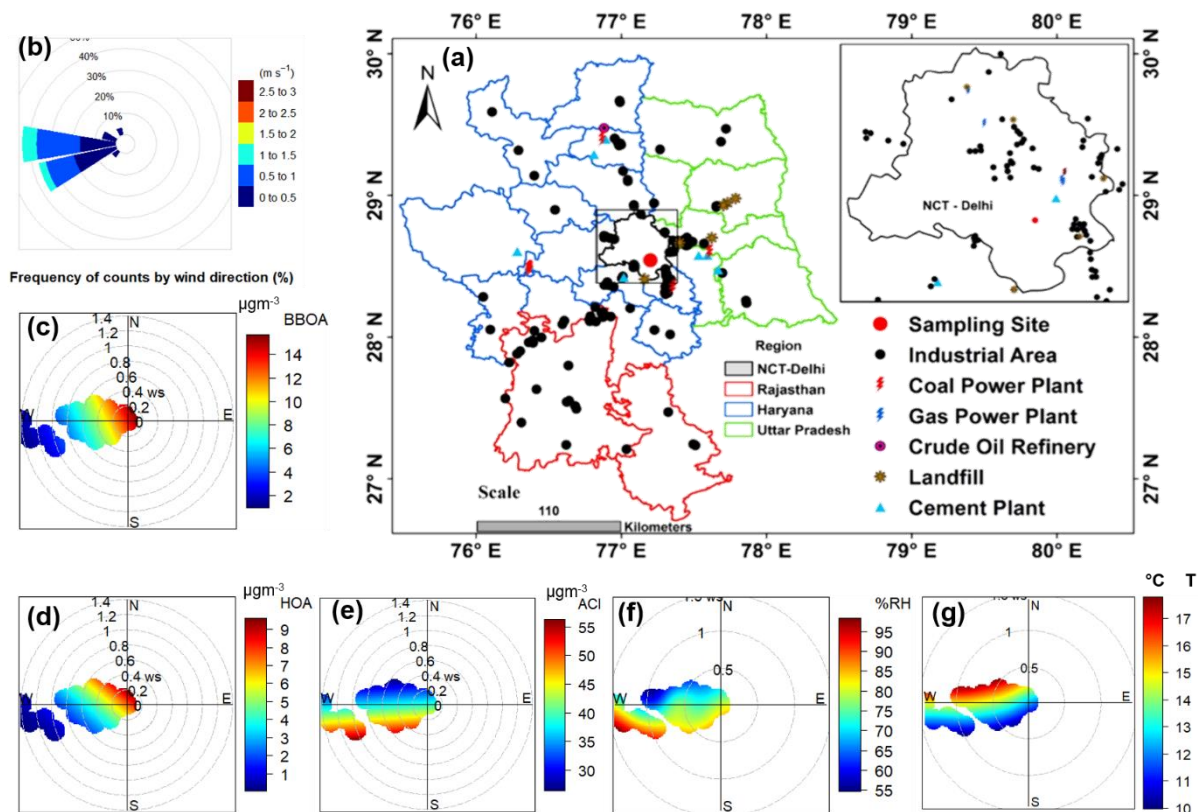
3.2.4.1 High-Cl (H-Cl) events

H-Cl events were selected as they correspond to a significant increase (>20%) in the fractional volume contribution of NH$_4$Cl (ε_{ACl}) in the PM$_1$ aerosol at the receptor site. During this period, the surface wind mainly came from the west, although it was also influenced by wind from the west-northwest, west-southwest, and southeast, as illustrated in Fig. 7b. The average geometric mean diameter of the PNSD was almost 64 nm,

473 indicating that nearby fresh emission sources impact the particles. In addition, the average concentration of SO_2,

474 NOx, and CO concentrations were at 3.6 ppb, 51.9 ppb, and 0.4 ppm, respectively. The potential contributors to

475 BBOA and HOA were from the WNW and SE directions, as demonstrated in the bipolar plot Fig. 7(c & d), and

476 appeared to originate from a local source. Among the inorganic species, ACl displayed a strong correlation with

477 ambient RH, as illustrated in Fig. 7e and f, suggesting that atmospheric gaseous HCl was neutralized by NH_3 gas

478 in the presence of atmospheric water content. HCl sources may include coal power plants, solid waste dumping

479 sites with burning trash, and industries in the W-WSW direction (Gani et al., 2019), as depicted in in Fig. 7a.

480 Trash burning in Delhi during winter may potentially dominate atmospheric high Cl events (Shukla et al., 2021;

481 Tobler et al., 2020). In addition, the bipolar plots (Fig. 7(e and f)) indicate that ACl formation occurs under high

482 relative humidity conditions associated with a relatively calm atmosphere, thereby triggering particles

483 hygroscopicity. This hypothesis is supported by the strong correlation between ALWC, as discussed in the

484 previous section. Moreover, as shown in Fig. 8a, the GF-PDF of particles of all sizes shows a relatively higher

485 fraction of secondary mode particles contributing. More hygroscopic particles ($HGF_{90\%}$ >1.2) accounted for higher

486 percentage of 42%, 47%, 50%, 74%, and 83% in particles ranging from 20nm to 200nm in size, respectively.

487 Therefore, ACl plays a significant role in increasing aerosol hygroscopicity, leading to the formation of fog/haze

488 under higher RH and colder atmospheric conditions.

489 Gunthe et al. (2021) observed that high local emissions of hydrochloric acid in Delhi during February-March are

490 partitioned into aerosol liquid water under high humidity conditions. This enhances the water uptake capacity of

491 aerosols, sustaining particle hygroscopic growth and resulting in fog/haze formation. Additionally, studies

492 worldwide on size-resolved hygroscopicity have observed Cl to be less than 1%, leading to the omission of ACl

493 as an aerosol constituent in the discussion. The current study did not find a strong correlation between κ with AS

494 or AN, which may be due to their association with larger particle sizes. Additionally, ACl may be associated with

495 particles of a comparatively smaller size ($\leq$ 200 nm). Furthermore, in the context of examining the influence of

496 air mass trajectories, we mapped the constituents of aerosols in association with air mass back trajectories using

497 PSCF to determine the potential area source contribution that may be influencing the aerosol evaluation processes,

498 specifically the aerosol's hygroscopicity. However, we did not find any back trajectories that influenced the

499 receptor site, as all trajectory endpoints were observed above the height of the planetary boundary layer.

500

Figure 7 Map of (a) Delhi showing various types of industries located in the region and nearby locations, (b) wind rose diagram and conditional bi-polar plots showing variation in mass concentration of (c) biomass burning OA (BBOA), (d) hydrocarbon like OA (HOA), (e) ammonium chloride (ACl), (f) % ambient relative humidity (RH), and (g) ambient temperature (T), with wind direction (WD) and wind speed (WS) during H-Cl events. A background map showing various industrial locations was adapted from Rai et al. (2020).

3.2.4.2 High biomass burning (H-BB) Events

During the initial period of the field campaign (1-12 February), there were instances of high BB events. However, H-BB events were generally observed during the midnight (01:00 hours) to morning (08:00 hours) or evening (20:00 hours) to midnight (01:00 hours), and occasionally from evening (21:00 hours) to morning (11:00 hours). The surface wind circulations were predominantly from the W, W-WNW, and W-WSW directions (refer to Fig. S9b). The aerosol in this study was primarily sourced from local emissions. The aerosol constituents were mainly associated with slower wind circulations from landfill sites, industrial areas, and coal power plants, as shown in Fig. S9a. The PSCF analysis was justified by considering 48-hour air mass back trajectories, as shown in Fig. S10. The average GMD of the PNSD was nearly 87 nm. Additionally, the mean concentration of SO_2, NOx, and CO were at 4.7 ppb, 124.1 ppb, and 1.5 ppm, respectively. Therefore, it is possible that BBOA was contributed from the open local biomass burning activities at landfill sites or others sources. The H-BB event showed that

22

organic aerosol confined the largest fraction of BBOA, at 39%, followed by HOA at 28%. Fig. S9 (b, c, and d) clearly shows that BBOA and HOA have similar local source profiles but differ from the ACl source. Additionally, ACl was not found to have a strong association with ambient RH, but it was associated with emissions from a nearby coal power plant. However, the 48-hour air mass back trajectories indicate that the current city is also influenced by air masses from certain parts of Uttar Pradesh, Punjab, and Haryana. These states are potential hubs for crop residue burning, industrial activities and brick kilns, which contribute significantly to the presence of organic aerosols in PM_1, particularly during winter. The H-BB event captured a significant volume fraction, 71%, of OA in PM_1. BBOA contributed almost 39%, as shown in Fig. 9. A lower inorganic to OA ratio was a potential factor in decreasing the aerosol hygroscopicity during H-BB events. Additionally, the contribution of primary organic aerosol was enhanced during this event and, on average, increased to 67%. The hygroscopicity of the aerosol is inversely affected by organic aerosol loading. This observation was also reported by Mandariya et al. (2020) in Kanpur. The authors suggested that the hygroscopicity of the aerosol is adversely affected by primary biomass burning (BBOA) and hydrocarbon-like OA. BBOA was found to have a strong negative correlation with the hygroscopicity of 200 nm particles, supporting the conclusion. Apart from this, the Nucleation size particle (20 nm) exhibited a hygroscopicity parameter of 0.02 ± 0.02 with a mono mode GF-PDF with the unit mode (Fig. 8b) and consisted of $83.7 \pm 18.6\%$ nearly hydrophobic particles. Additionally, as the aerosol size increased, the hygroscopicity parameter ($\kappa_{H\text{-}TDMA\_90\%}$) significantly ($p<0.05$) increased due to the contribution of relatively secondary aerosol particles (GF>1.2) with increasing aerosol size. Approximately 54% of the accumulation size aerosol with a diameter of 100 nm is contributed by nearly hydrophobic particles (GF<1.2), while the remaining 46% is contributed by more hygroscopic particles (GF>1.2).

3.2.4.3 High-HOA (H-HOA) Events
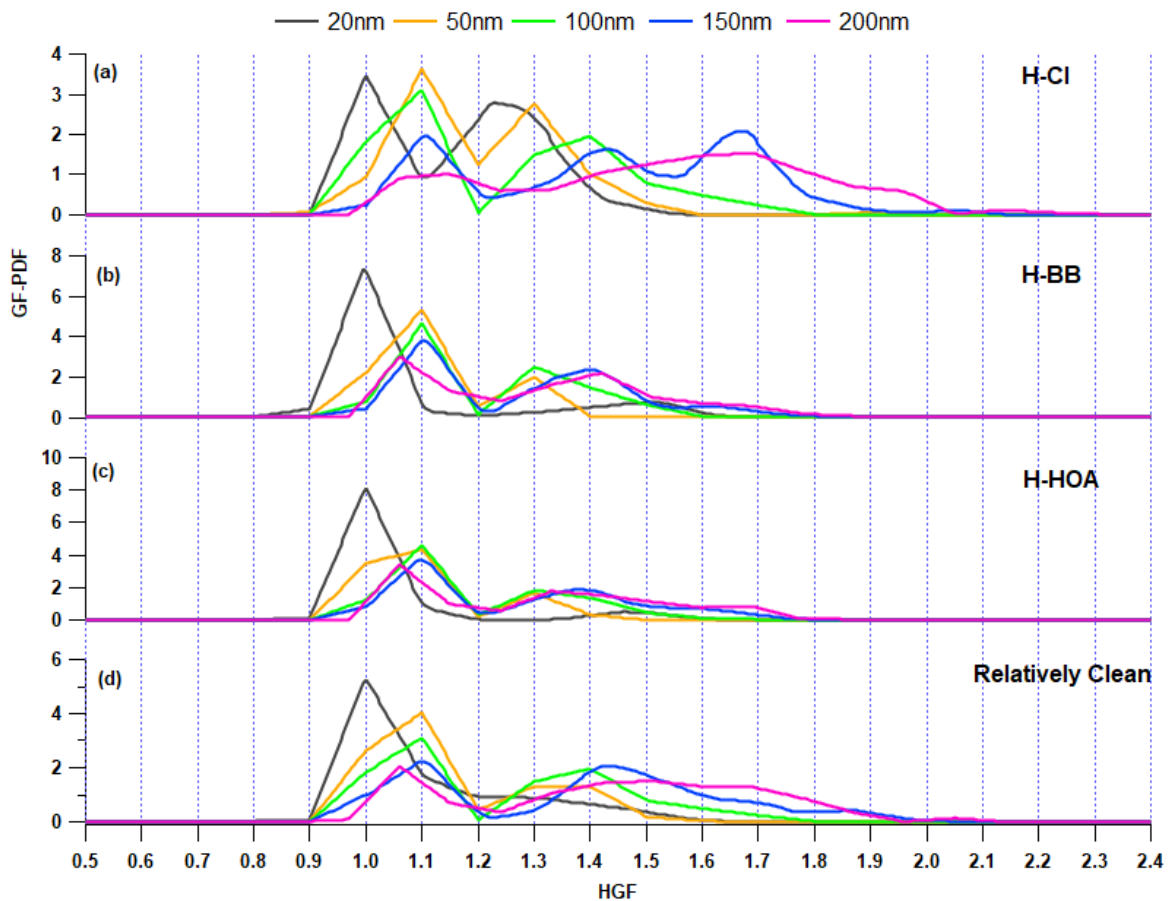
H-HOA events were identified based on the considerable mass concentration and fraction of HOA in the organic aerosol. These periods were generally noted from19:00 hr to 09:00 hr the following morning during February 22-23, February 26-27 February, March 4, and March 7-8, as indicated in Fig. 2. The average geometric mean diameter of the particle number size distribution was nearly 80 nm. Additionally, the mean concentrations of SO_2, NOx, and CO 4.3 ppb, 136.7 ppb, and 1.1 ppm, respectively. The potential impact of long-range transported aerosol was explored using PSCF. Air masses over Delhi, Haryana, and Uttar Pradesh were found to be potentially associated with hydrocarbon-like organic aerosols (Fig. S11). BBOA also followed a similar path as HOA. However, the potential area source of ACl was the nearby region of Delhi and Haryana. The loading of HOA was significantly ($p<0.05$) higher than in H-BB, H-Cl and Clean periods. However, emission sources were different

548   during both H-HOA and H-BB periods. HOA may be a critical constituent in modulating aerosol hygroscopicity

549   during these events, as it has been identified as a potential contributor to OA. HOA is typically considered

550   hydrophobic (Duplissy et al., 2011), and therefore, its elevated contribution (41%) to OA could be responsible for

551   the lower κ observed during these events. The overall hygroscopicity of particles with sizes of 20, 50, 100, 150,

552   and 200 nm was recorded as 0.01 ± 0.01, 0.06 ± 0.03, 0.11 ± 0.03, 0.14 ± 0.04, and 0.17 ± 0.05, respectively. The

553   lower hygroscopicity of particles may be attributed to the predominant fractional contribution of primary aerosol

554   particles (GF<1.2), as illustrated in Fig. 8(c). In general, OA constitutes the majority of the PM_1, with primary

555   OA accounting for approximately 60% of the OA. However, the relative increase in the contribution of other more

556   hygroscopic constituents, such as secondary organic aerosol (LO-OOA and MO-OOA), ACl, and AS, in the

557   aerosol may help to balance the negative impact of high-HOA, which is limited by κ.

558   **3.2.4.5 Relatively Clean Period**

559   Clean events were recorded on February 24th, 25th, and March 5th-7th. The clean duration was from 9 PM to 11

560   AM. E and S-E winds dominated the relatively clean period, but pollution was associated with calm winds, as

561   shown in Fig. S12. The average GMD of the PNSD was nearly 54 nm. Additionally, the mean concentrations of

562   SO_2, NOx, and CO concentrations were at 4.2 ppb, 43.2 ppb, and 0.4 ppm, respectively. Similar sources were

563   found for BBOA, HOA, and ACl, and they were all strongly associated with ambient relative humidity. The mean

564   concentrations of organic aerosol, ACl, AN, and AS were 11.0 ± 6.4, 1.4 ± 1.1, 3.0 ± 1.5, and 4.4 ± 2.2 μgm^{-3},

565   respectively. These mass concentrations were significantly lower than in other specified periods. However, OA

566   was still the dominant species, comprising 56% of the PM_1 volume, as shown in Fig. 9. Of all the factors

567   contributing to OA, HOA was the dominant, accounting for 33%. However, secondary organic aerosol accounted

568   for the majority of OA at 54.4%. Secondary OA is characterize by a relatively higher degree of oxidation, which

569   positively affects OA hygroscopicity (Kim et al., 2017; Richard et al., 2011; Wu et al., 2013a). The mean

570   hygroscopicity of particles with diameters of 20, 50, 100, 150, and 200 nm during the Clean period were observed

571   to be 0.03 ± 0.02, 0.09 ± 0.04, 0.14 ± 0.06, 0.22 ± 0.09, and 0.27 ± 0.07, respectively. These values were

572   significantly ($p<0.05$) different from each other. However, the hygroscopicity of the 200 nm accumulation

573   particles was not significantly ($p>0.05$) higher than that of the 150 nm particles. The increase in hygroscopicity

574   as particle size increases from 20 to 200 nm can also be attributed to the greater proportion of more hygroscopic

575   particles (GF>1.2) compared to nearly hydrophobic or less hygroscopic particles (GF<1.2) (refer Fig. 8d). The

576   nucleation particles, with a size of 20 nm, were mostly composed of less hygroscopic particles ($76.8 \pm 21.7\%$).

577   This indicates that there was an influence from fresh emission sources. On the other hand, Aitken (50 nm) and

578   Accumulation (200 nm) size aerosols had a lower percentage of less hygroscopic particles, with 69.3 ± 14.7 and

579   25.4 ± 10.8, respectively. These results suggest that accumulation-size aerosols dominated secondary aerosols,

580   which is also supported by their GF-PDF as shown in Fig. 8(d). Aerosol particles of nucleation size (20nm)

581   exhibited a nearly mono-modal GF-PDF with a mode of unit growth factor. In contrast, as the aerosol size

582   increased, the mode shifted towards the higher end and the GF-PDF shifted from unit to multi-mode.
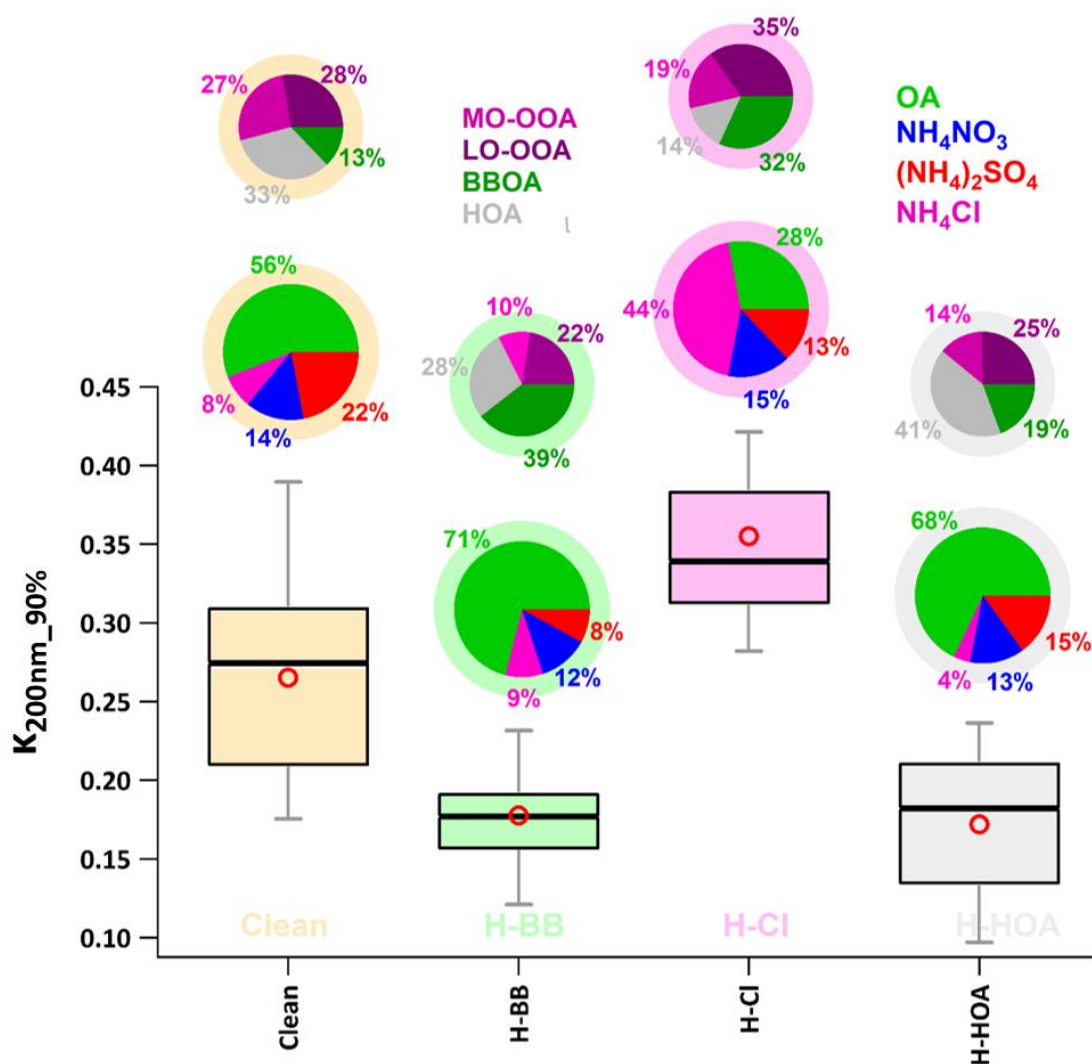

583

584   **Figure 8: Growth Factor Probability Density Function (GF-PDF) of 20, 50, 100, 150, and 200 nm aerosol particles for**

585   **the (a) H-Cl, (b) H-BB, (c) H-HOA, and (d) relatively clean periods.**

586   **3.2.4.6 Comparison of κ for different events**

587   We compared the hygroscopicity of aerosols during different periods using a 200 nm particle size that represents

588   the bulk aerosol chemical composition. Additionally, in this study, the mode of the particle-volume size

589   distribution ranged from 400 nm to 600 nm in dry mobility diameter. Therefore, 200 nm particles are the best

590   choice for comparing hygroscopicity parameters among different periods, considering bulk aerosol composition.

591   Additionally, a good Pearson's r value of 0.76 was found between $\kappa_{200nm\_90\%}$ and $\kappa_{chem\_90\%}$, which were derived

592   from the chemical composition of dry PM_1 particles measured by the ACSM using the ZSR mixing rule (Stokes

593   and Robinson, 1966). This supports our decision to consider 200 particles for comparison.

594   The event labeled H-Cl exhibited the highest value (0.36 ± 0.06) of $\kappa_{200nm\_90\%}$ compared to the events labeled H-

595   BB (0.18 ± 0.04), H-HOA (0.17 ± 0.05), and relatively Clean (0.27 ± 0.07), as shown in Fig. 9. Additionally, the

596   average $\kappa_{200nm\_90\%}$ value for the H-Cl event was significantly ($p<0.05$) higher than that of the other events. A

597   significant increase in Cl emissions in the Delhi region could lead to a substantial increase in the aerosol liquid

598   water content. This increase in water content could result in higher aerosol hygroscopicity, which could further

599   enhance cloud condensation nuclei formation. This, in turn, could potentially trigger haze/fog events in Delhi

600   NCR (Gunthe et al., 2021). Controlling open trash/waste burning in the region could help minimize Cl emissions,

601   which in turn could rduce the possibility of haze/fog formation during high atmospheric conditions. However,

602   there was no significant difference ($p>0.05$) in $\kappa_{200nm\_90\%}$ values between H-BB and H-HOA events, possibly due

603   to relative changes in primary, secondary OA, and inorganic species. In H-HOA events, the negative effect of a

604   significantly higher fractional contribution of HOA to OA (41%) possibly balances with a positive impact of a

605   7% increase in secondary OA relative to H-BB. Several worldwide studies (Jimenez et al., 2009; Mandariya et

606   al., 2019; Sun et al., 2013) have reported that secondary organic aerosol is associated with a higher O/C ratio.

607   Additionally, several studies have found a positive correlation between the O/C ratio and κ (Jimenez et al., 2009;

608   Kim et al., 2020), as described earlier. Furthermore, a 5% decrease in ACl during H-HOA events may be offset

609   by a 7% increase in AS fraction during H-BB events. Overall, the relative changes in aerosol constituents resulted

610   in insignificant changes in κ during H-BB and H-HOA periods. However, H-BB and H-HOA events showed

611   significantly ($p<0.05$) lower hygroscopicity compared to a relatively cleaner atmosphere. The aerosol associated

612   with relatively cleaner events had a higher inorganic-to-organic ratio. Additionally, during clean periods, the

613   aerosol consisted of a significantly higher fraction of secondary organic aerosol. This could be the reason for the

614   higher hygroscopicity associated with organic aerosol compared to other events. Studies worldwide (Aiken et al.,

615   2008; Cerully et al., 2015b; Chakraborty et al., 2016b; Mandariya et al., 2019) have reported that organic aerosol

616   loading has an inverse impact on the oxidation/aging process of OA. This results in higher hygroscopicity during

617   relatively cleaner periods.

Figure 9: Box plot showing variation in H-TDMA measured hygroscopic parameter of 200 nm size particles $\kappa_{\text{H-TDMA}}$ ($\kappa_{\text{200nm\_90\%}}$) in high biomass burning (H-BB), high-chloride (H-Cl), and high-hydrocarbon like organic aerosol (H-HOA) events. Different colors represent respective events in the plot. A bigger pie chart represents the overall average volume fractional contribution of various aerosol species indicated by color-coding. In addition, minor pie charts described the event average mass fractional contribution of different OA species in OA. Diffused ring color of the pie chart displays the respective event.

4. Conclusions

The study examined the hygroscopicity of aerosol particles of various sizes (Nucleation - 20 nm, Aitken - 50 nm, and Accumulation - 150 and 200 nm) in Delhi during the winter months of February-March 2020. The research also identified differences in hygroscopicity, particularly in aerosols with higher levels of chloride, biomass burning, and hydrocarbon-like organic components. Delhi is known as one of the most polluted cities, particularly

630 during winter haze and fog events when it often experiences high levels of chloride pollution. This study reports

631 on the temporal variations in size-specific hygroscopic parameters ($\kappa_{H\text{-}TDMA\_90\%}$) under sub-saturated conditions

632 (90% RH) in Delhi for the first time. Additionally, it presents the hygroscopicity of nucleation and Aitken mode

633 particles using HTDMA for the first time in India.

634 The $\kappa_{H\text{-}TDMA\_90\%}$ values observed for aerosol particles of 20 nm, 50 nm, 100 nm, 150 nm, and 200 nm ranged from

635 0.00 to 0.11 (with an average of 0.03 ± 0.02), 0.05 to 0.22 (0.11 ± 0.03), 0.05 to 0.30 (0.14 ± 0.04), 0.05 to 0.41

636 (0.18 ± 0.06), and 0.05 to 0.56 (0.22 ± 0.07), respectively. During the study period, it was observed that the

637 average hygroscopicity parameter increased significantly with the size of the particles ($p < 0.05$). The diurnal

638 variations of $\kappa_{20nm\_90\%}$ and $\kappa_{50nm\_90\%}$ were dynamic, while larger accumulation mode particles showed a flatter

639 diurnal pattern. This was due to the positive and negative effects of changes in the volume fraction of NH_4Cl and

640 organic aerosol in the aerosol with increasing particle size. The variation in $\kappa_{200nm\_90\%}$ was primarily associated

641 with fluctuations in NH_4Cl and OA, rather than $(NH_4)_2SO_4$.

642 Pollution episodes were mainly linked to local biomass burning and industrial and waste-burning emissions in

643 Delhi and nearby regions. The study primarily focused on the impacts of high biomass burning (H-BB), high

644 hydrocarbon-like OA (H-HOA), and high chloride emissions (H-Cl) on aerosol hygroscopicity and compared

645 them to cleaner periods. The period with H-Cl exhibited significantly higher hygroscopicity (0.35 ± 0.06)

646 compared to the periods with H-BB (0.18 ± 0.04), H-HOA (0.17 ± 0.05), and the relatively cleaner period (0.27

647 ± 0.07). However, H-BB and H-HOA showed no significant difference in hygroscopicity but displayed lower

648 hygroscopicity compared to the cleaner periods. This could be attributed to lower levels of organic aerosols and

649 a higher ratio of inorganic-to-organic aerosol in the aerosol. The study found that an increase of 10% increase in

650 chloride aerosol (ammonium chloride) significantly increased hygroscopicity, resulting in approximately 3 µg m^{-}

651 ^{3} higher aerosol liquid water content during high chloride events. This 10% increase in a high-volume fraction of

652 ammonium chloride in aerosol significantly ($p < 0.05$) enhanced aerosol hygroscopicity by 0.0041. The research

653 indicates that chloride emissions are a significant concern in Delhi. These emissions enhance aerosol

654 hygroscopicity, promote cloud formation during winter days, and contribute to fog and haze in the region. High

655 levels of chloride in aerosols counteract the negative impact of high organic aerosol loading on cloud condensation

656 nuclei activity. The study suggests that controlling open burning of waste materials could help reduce haze and

657 fog events in Delhi during the winter months.

658 **Supporting Information**

659 Supplementary pieces of information are mentioned in the supplementary file.

660 **Data availability.** Data can be accessed at the following repository:

661 https://web.iitd.ac.in/~gazala/publications.html (Mandariya et al., 2023).

662 **Author contributions.** AKM: conceptualization, HTDMA data analysis, investigation, methodology, writing

663 (original draft and review and editing). AA: operated aerosol instrumentation and collection of data on-board in

664 Delhi, analysis of MPSS data, conceptualization, review and editing. MH: help in data collection. NAB: ACSM

665 operation and data collection. KP: ACSM data analysis and PMF analysis. JA: providing ACSM, review, and

666 editing. LHR: ACSM, review, and editing. AW: experiment design, project administration, supervision, review,

667 and editing. GH: operated aerosol instrumentation and collection of data on-board in Delhi, data analysis,

668 methodology, funding acquisition, project administration, supervision, review and editing.

669 **Corresponding Author**

670 Gazala Habib (gazalahabib@civil.iitd.ac.in) and Alfred Wiedensohler (ali@tropos.de)

671 **Competing interests**

672 The authors declare that they have no conflict of interest.

673

677 **REFERENCES**

678 Achtert, P., Birmili, W., Nowak, A., Wehner, B., Wiedensohler, A., Takegawa, N., Kondo, Y., Miyazaki, Y., Hu,
679 M. and Zhu, T.: Hygroscopic growth of tropospheric particle number size distributions over the North China Plain,
680 J. Geophys. Res., 114(8), D00G07, doi:10.1029/2008JD010921, 2009.

681 Aiken, A. C., Decarlo, P. F., Kroll, J. H., Worsnop, D. R., Huffman, J. A., Docherty, K. S., Ulbrich, I. M., Mohr,
682 C., Kimmel, J. R., Sueper, D., Sun, Y., Zhang, Q., Trimborn, A., Northway, M., Ziemann, P. J., Canagaratna, M.
683 R., Onasch, T. B., Alfarra, M. R., Prevot, A. S. H., Dommen, J., Duplissy, J., Metzger, A., Baltensperger, U. and
684 Jimenez, J. L.: O/C and OM/OC ratios of primary, secondary, and ambient organic aerosols with high-resolution
685 time-of-flight aerosol mass spectrometry, Environ. Sci. Technol., 42(12), 4478–4485, doi:10.1021/es703009q,
686 2008.

687 Albrecht, B. A.: Aerosols, Cloud Microphysics, and Fractional Cloudiness, Science (80-.)., 245(4923), 1227–
688 1230, doi:10.1126/science.245.4923.1227, 1989.

689 Arub, Z., Bhandari, S., Gani, S., Apte, J. S., Hildebrandt Ruiz, L. and Habib, G.: Air mass physiochemical

690 characteristics over New Delhi: impacts on aerosol hygroscopicity and cloud condensation nuclei (CCN)
691 formation, Atmos. Chem. Phys., 20(11), 6953–6971, doi:10.5194/acp-20-6953-2020, 2020.

692 Bhandari, S., Gani, S., Patel, K., Wang, D. S., Soni, P., Arub, Z., Habib, G., Apte, J. S. and Hildebrandt Ruiz, L.:
693 Sources and atmospheric dynamics of organic aerosol in New Delhi, India: insights from receptor modeling,
694 Atmos. Chem. Phys., 20(2), 735–752, doi:10.5194/acp-20-735-2020, 2020.

695 Bhattu, D. and Tripathi, S. N.: CCN closure study: Effects of aerosol chemical composition andmixing state, J.
696 Geophys. Res., 120(2), 766–783, doi:10.1002/2014JD021978, 2015.

697 Bhattu, D., Tripathi, S. N. and Chakraborty, A.: Deriving aerosol hygroscopic mixing state from size-resolved
698 CCN   activity   and   HR-ToF-AMS   measurements,   Atmos.   Environ.,   142,   57–70,
699 doi:10.1016/j.atmosenv.2016.07.032, 2016.

700 Cerully, K. M., Bougiatioti, A., Hite, J. R., Guo, H., Xu, L., Ng, N. L., Weber, R. and Nenes, A.: On the link
701 between hygroscopicity, volatility, and oxidation state of ambient and water-soluble aerosols in the southeastern
702 United States, Atmos. Chem. Phys., 15(15), 8679–8694, doi:10.5194/acp-15-8679-2015, 2015a.

703 Cerully, K. M., Bougiatioti, A., Hite, J. R., Guo, H., Xu, L., Ng, N. L., Weber, R. and Nenes, A.: On the link
704 between hygroscopicity, volatility, and oxidation state of ambient and water-soluble aerosols in the southeastern
705 United States, Atmos. Chem. Phys., 15(15), 8679–8694, doi:10.5194/acp-15-8679-2015, 2015b.

706 Chakraborty, A., Gupta, T. and Tripathi, S. N.: Combined effects of organic aerosol loading and fog processing
707 on organic aerosols oxidation, composition, and evolution, Sci. Total Environ., 573, 690–698,
708 doi:10.1016/j.scitotenv.2016.08.156, 2016a.

709 Chakraborty, A., Gupta, T. and Tripathi, S. N.: Combined effects of organic aerosol loading and fog processing
710 on organic aerosols oxidation, composition, and evolution, Sci. Total Environ., 573, 690–698,
711 doi:10.1016/j.scitotenv.2016.08.156, 2016b.

712 Chen, Y., Wang, Y., Nenes, A., Wild, O., Song, S., Hu, D., Liu, D., He, J., Hildebrandt Ruiz, L., Apte, J. S.,
713 Gunthe, S. S. and Liu, P.: Ammonium Chloride Associated Aerosol Liquid Water Enhances Haze in Delhi, India,
714 Environ. Sci. Technol., 56(11), 7163–7173, doi:10.1021/ACS.EST.2C00650, 2022.

715 Draxler, Roland R., Hess, G. D.: Descrpition of the HYSPLIT_4 Modeling System, NOAA Techincal Memo.
716 ERL ARL-224, (October 2004), 28 [online] Available from: http://arlsun.arlhq.noaa.gov/documents/reports/arl-
717 224.pdf%5Cnhttp://www.ciecem.uhu.es/hysplitweb08/document/arl-224.pdf, 1997.

718 Duplissy, J., De Carlo, P. F., Dommen, J., Alfarra, M. R., Metzger, A., Barmpadimos, I., Prevot, A. S. H.,
719 Weingartner, E., Tritscher, T., Gysel, M., Aiken, A. C., Jimenez, J. L., Canagaratna, M. R., Worsnop, D. R.,
720 Collins, D. R., Tomlinson, J. and Baltensperger, U.: Relating hygroscopicity and composition of organic aerosol
721 particulate matter, Atmos. Chem. Phys., 11(3), 1155–1165, doi:10.5194/acp-11-1155-2011, 2011.

722 Enroth, J., Mikkilä, J., Németh, Z., Kulmala, M. and Salma, I.: Wintertime hygroscopicity and volatility of
723 ambient urban aerosol particles, Atmos. Chem. Phys., 18(7), 4533–4548, doi:10.5194/acp-18-4533-2018, 2018.

724 Ervens, B., Turpin, B. J. and Weber, R. J.: Secondary organic aerosol formation in cloud droplets and aqueous
725 particles (aqSOA): A review of laboratory, field and model studies, Atmos. Chem. Phys., 11(21), 11069–11102,
726 doi:10.5194/acp-11-11069-2011, 2011.

727 Fan, X., Liu, J., Zhang, F., Chen, L., Collins, D., Xu, W., Jin, X., Ren, J., Wang, Y., Wu, H., Li, S., Sun, Y. and
728 Li, Z.: Contrasting size-resolved hygroscopicity of fine particles derived by HTDMA and HR-ToF-AMS
729 measurements between summer and winter in Beijing: the impacts of aerosol aging and local emissions, Atmos.
730 Chem. Phys., 20(2), 915–929, doi:10.5194/acp-20-915-2020, 2020.

731 Fountoukis, C. and Nenes, A.: ISORROPIAII: A computationally efficient thermodynamic equilibrium model for
732 K^+-Ca^{2+}-Mg^{2+}-NH_4^+-Na^+-SO_4^{2-}-NO_3^--Cl^--H_2O aerosols,   Atmos.   Chem.   Phys.,   7(17),   4639–4659,
733 doi:10.5194/acp-7-4639-2007, 2007.

734 Gani, S., Bhandari, S., Seraj, S., Wang, D. S., Patel, K., Soni, P., Arub, Z., Habib, G., Hildebrandt Ruiz, L. and

735 Apte, J. S.: Submicron aerosol composition in the world's most polluted megacity: the Delhi Aerosol Supersite
736 study, Atmos. Chem. Phys., 19(10), 6843–6859, doi:10.5194/acp-19-6843-2019, 2019.

737 Gunthe, S. S., Rose, D., Su, H., Garland, R. M., Achtert, P., Nowak, A., Wiedensohler, A., Kuwata, M., Takegawa,
738 N., Kondo, Y., Hu, M., Shao, M., Zhu, T., Andreae, M. O. and Pöschl, U.: Cloud condensation nuclei (CCN) from
739 fresh and aged air pollution in the megacity region of Beijing, Atmos. Chem. Phys., 11(21), 11023–11039,
740 doi:10.5194/acp-11-11023-2011, 2011.

741 Gunthe, S. S., Liu, P., Panda, U., Raj, S. S., Sharma, A., Darbyshire, E., Reyes-Villegas, E., Allan, J., Chen, Y.,
742 Wang, X., Song, S., Pöhlker, M. L., Shi, L., Wang, Y., Kommula, S. M., Liu, T., Ravikrishna, R., McFiggans, G.,
743 Mickley, L. J., Martin, S. T., Pöschl, U., Andreae, M. O. and Coe, H.: Enhanced aerosol particle growth sustained
744 by high continental chlorine emission in India, Nat. Geosci., 14(2), 77–84, doi:10.1038/s41561-020-00677-x,
745 2021.

746 Gupta, T. and Mandariya, A.: Sources of submicron aerosol during fog-dominated wintertime at Kanpur, Environ.
747 Sci. Pollut. Res., 20(8), doi:10.1007/s11356-013-1580-6, 2013.

748 Gysel, M., Crosier, J., Topping, D. O., Whitehead, J. D., Bower, K. N., Cubison, M. J., Williams, P. I., Flynn, M.
749 J., McFiggans, G. B. and Coe, H.: Closure study between chemical composition and hygroscopic growth of
750 aerosol particles during TORCH2, Atmos. Chem. Phys., 7(24), 6131–6144, doi:10.5194/acp-7-6131-2007, 2007.

751 Gysel, M., McFiggans, G. B. and Coe, H.: Inversion of tandem differential mobility analyser (TDMA)
752 measurements, J. Aerosol Sci., 40(2), 134–151, doi:10.1016/j.jaerosci.2008.07.013, 2009.

753 Hallquist, M., Wenger, J. C., Baltensperger, U., Rudich, Y., Simpson, D., Claeys, M., Dommen, J., Donahue, N.
754 M., George, C., Goldstein, A. H., Hamilton, J. F., Herrmann, H., Hoffmann, T., Linuma, Y., Jang, M., Jenkin, M.
755 E., Jimenez, J. L., Kiendler-Scharr, A., Maenhaut, W., McFiggans, G., Mentel, T. F., Monod, A., Prévot, A. S.
756 H., Seinfeld, J. H., Surratt, J. D., Szmigielski, R. and Wildt, J.: The formation, properties and impact of secondary
757 organic aerosol: current and emerging issues, Atmos. Chem. Phys., 9(November 2008), 5155–5236, 2009.

758 Hong, J., Häkkinen, S. A. K., Paramonov, M., Äijälä, M., Hakala, J., Nieminen, T., Mikkilä, J., Prisle, N. L.,
759 Kulmala, M., Riipinen, I., Bilde, M., Kerminen, V. M. and Petäjä, T.: Hygroscopicity, CCN and volatility
760 properties of submicron atmospheric aerosol in a boreal forest environment during the summer of 2010, Atmos.
761 Chem. Phys., 14(9), 4733–4748, doi:10.5194/acp-14-4733-2014, 2014.

762 Hong, J., Kim, J., Nieminen, T., Duplissy, J., Ehn, M., Äijälä, M., Hao, L. Q., Nie, W., Sarnela, N., Prisle, N. L.,
763 Kulmala, M., Virtanen, A., Petäjä, T. and Kerminen, V. M.: Relating the hygroscopic properties of submicron
764 aerosol to both gas- and particle-phase chemical composition in a boreal forest environment, Atmos. Chem. Phys.,
765 15(20), 11999–12009, doi:10.5194/acp-15-11999-2015, 2015.

766 Hong, J., Xu, H., Tan, H., Yin, C., Hao, L., Li, F., Cai, M., Deng, X., Wang, N., Su, H., Cheng, Y., Wang, L.,
767 Petäjä, T. and Kerminen, V. M.: Mixing state and particle hygroscopicity of organic-dominated aerosols over the
768 Pearl River Delta region in China, Atmos. Chem. Phys., 18(19), 14079–14094, doi:10.5194/acp-18-14079-2018,
769 2018.

770 Hu, D., Chen, J., Ye, X., Li, L. and Yang, X.: Hygroscopicity and evaporation of ammonium chloride and
771 ammonium nitrate: Relative humidity and size effects on the growth factor, Atmos. Environ., 45(14), 2349–2355,
772 doi:10.1016/j.atmosenv.2011.02.024, 2011.
773

774 Intergovernmental Panel on Climate Change: Climate Change 2021 – The Physical Science Basis, Cambridge
775 University Press., 2023.

776 Jimenez, J. L., Canagaratna, M. R., Donahue, N. M., Prevot, A. S. H., Zhang, Q., Kroll, J. H., DeCarlo, P. F.,
777 Allan, J. D., Coe, H., Ng, N. L., Aiken, A. C., Docherty, K. S., Ulbrich, I. M., Grieshop, A. P., Robinson, A. L.,
778 Duplissy, J., Smith, J. D., Wilson, K. R., Lanz, V. A., Hueglin, C., Sun, Y. L., Tian, J., Laaksonen, A., Raatikainen,
779 T., Rautiainen, J., Vaattovaara, P., Ehn, M., Kulmala, M., Tomlinson, J. M., Collins, D. R., Cubison, M. J., Dunlea,
780 E. J., Huffman, J. A., Onasch, T. B., Alfarra, M. R., Williams, P. I., Bower, K., Kondo, Y., Schneider, J.,
781 Drewnick, F., Borrmann, S., Weimer, S., Demerjian, K., Salcedo, D., Cottrell, L., Griffin, R., Takami, A.,
782 Miyoshi, T., Hatakeyama, S., Shimono, A., Sun, J. Y., Zhang, Y. M., Dzepina, K., Kimmel, J. R., Sueper, D.,

783 Jayne, J. T., Herndon, S. C., Trimborn, A. M., Williams, L. R., Wood, E. C., Middlebrook, A. M., Kolb, C. E.,
784 Baltensperger, U. and Worsnop, D. R.: Evolution of organic aerosols in the atmosphere, Science (80-.).,
785 326(5959), 1525–1529, doi:10.1126/science.1180353, 2009.

786 Kawana, K., Nakayama, T. and Mochida, M.: Hygroscopicity and CCN activity of atmospheric aerosol particles
787 and their relation to organics: Characteristics of urban aerosols in Nagoya, Japan, J. Geophys. Res. Atmos., 121(8),
788 4100–4121, doi:10.1002/2015JD023213, 2016.

789 Kecorius, S., Vogl, T., Paasonen, P., Lampilahti, J., Rothenberg, D., Wex, H., Zeppenfeld, S., Van Pinxteren, M.,
790 Hartmann, M., Henning, S., Gong, X., Welti, A., Kulmala, M., Stratmann, F., Herrmann, H. and Wiedensohler,
791 A.: New particle formation and its effect on cloud condensation nuclei abundance in the summer Arctic: a case
792 study in the Fram Strait and Barents Sea, Atmos. Chem. Phys, 19, 14339–14364, doi:10.5194/acp-19-14339-2019,
793 2019.

794 Kim, N., Park, M., Yum, S. S., Park, J. S., Song, I. H., Shin, H. J., Ahn, J. Y., Kwak, K. H., Kim, H., Bae, G. N.
795 and Lee, G.: Hygroscopic properties of urban aerosols and their cloud condensation nuclei activities measured in
796 Seoul during the MAPS-Seoul campaign, Atmos. Environ., 153, 217–232, doi:10.1016/j.atmosenv.2017.01.034,
797 2017.

798 Kim, N., Yum, S. S., Park, M., Park, J. S., Shin, H. J. and Ahn, J. Y.: Hygroscopicity of urban aerosols and its
799 link to size-resolved chemical composition during spring and summer in Seoul, Korea, Atmos. Chem. Phys.,
800 20(19), 11245–11262, doi:10.5194/acp-20-11245-2020, 2020.

801 Kitamori, Y., Mochida, M. and Kawamura, K.: Assessment of the aerosol water content in urban atmospheric
802 particles by the hygroscopic growth measurements in Sapporo, Japan, Atmos. Environ., 43(21), 3416–3423,
803 doi:10.1016/j.atmosenv.2009.03.037, 2009.

804 Kroll, J. H., Donahue, N. M., Jimenez, J. L., Kessler, S. H., Canagaratna, M. R., Wilson, K. R., Altieri, K. E.,
805 Mazzoleni, L. R., Wozniak, A. S., Bluhm, H., Mysak, E. R., Smith, J. D., Kolb, C. E. and Worsnop, D. R.: Carbon
806 oxidation state as a metric for describing the chemistry of atmospheric organic aerosol, Nat. Chem., 3(2), 133–
807 139, doi:10.1038/nchem.948, 2011.

808 Li, H., Wang, Q., Shao, M., Wang, J., Wang, C., Sun, Y., Qian, X., Wu, H., Yang, M. and Li, F.: Fractionation of
809 airborne particulate-bound elements in haze-fog episode and associated health risks in a megacity of southeast
810 China, Environ. Pollut., 208, 655–662, doi:10.1016/j.envpol.2015.10.042, 2016.

811 Liu, J., Horowitz, L. W., Fan, S., Carlton, A. G. and Levy, H.: Global in-cloud production of secondary organic
812 aerosols: Implementation of a detailed chemical mechanism in the GFDL atmospheric model AM3, J. Geophys.
813 Res. Atmos., 117(D15), n/a-n/a, doi:10.1029/2012JD017838, 2012.

814 Lohmann, U. and Feichter, J.: Global indirect aerosol effects: a review, Atmos. Chem. Phys., 5(3), 715–737,
815 doi:10.5194/acp-5-715-2005, 2005.

816 Mandariya, A. K., Gupta, T. and Tripathi, S. N.: Effect of aqueous-phase processing on the formation and
817 evolution of organic aerosol (OA) under different stages of fog life cycles, Atmos. Environ., 206(November 2018),
818 60–71, doi:10.1016/j.atmosenv.2019.02.047, 2019.

819 Mandariya, A. K., Tripathi, S. N., Gupta, T. and Mishra, G.: Wintertime hygroscopic growth factors (HGFs) of
820 accumulation mode particles and their linkage to chemical composition in a heavily polluted urban atmosphere of
821 Kanpur at the Centre of IGP, India: Impact of ambient relative humidity, Sci. Total Environ., 704, 135363,
822 doi:10.1016/j.scitotenv.2019.135363, 2020a.

823 Mandariya, A. K., Tripathi, S. N., Gupta, T. and Mishra, G.: Wintertime hygroscopic growth factors (HGFs) of
824 accumulation mode particles and their linkage to chemical composition in a heavily polluted urban atmosphere of
825 Kanpur at the Centre of IGP, India: Impact of ambient relative humidity, Sci. Total Environ., 704,
826 doi:10.1016/j.scitotenv.2019.135363, 2020b.

827 Massling, A., Leinert, S., Wiedensohler, A. and Covert, D.: Hygroscopic growth of sub-micrometer and one-
828 micrometer aerosol particles measured during ACE-Asia, Atmos. Chem. Phys, 7, 3249–3259 [online] Available
829 from: www.atmos-chem-phys.net/7/3249/2007/ (Accessed 30 October 2022), 2007.

32

830   Maßling, A., Wiedensohler, A., Busch, B., Neusüß, C., Neusüß, N., Quinn, P., Bates, T. and Covert, D.:
831   Atmospheric Chemistry and Physics Hygroscopic properties of different aerosol types over the Atlantic and Indian
832   Oceans, Atmos. Chem. Phys, 3, 1377–1397 [online] Available from: www.atmos-chem-phys.org/acp/3/1377/
833   (Accessed 30 October 2022), 2003.

834   Massoli, P., Lambe, A. T., Ahern, A. T., Williams, L. R., Ehn, M., Mikkilä, J., Canagaratna, M. R., Brune, W. H.,
835   Onasch, T. B., Jayne, J. T., Petäjä, T., Kulmala, M., Laaksonen, A., Kolb, C. E., Davidovits, P. and Worsnop, D.
836   R.: Relationship between aerosol oxidation level and hygroscopic properties of laboratory generated secondary
837   organic aerosol (SOA) particles, Geophys. Res. Lett., 37(24), 1–5, doi:10.1029/2010GL045258, 2010.

838   McFiggans, G., Artaxo, P., Baltensperger, U., Coe, H., Facchini, M. C., Feingold, G., Fuzzi, S., Gysel, M.,
839   Laaksonen, A., Lohmann, U., Mentel, T. F., Murphy, D. M., O'Dowd, C. D., Snider, J. R. and Weingartner, E.:
840   The effect of physical and chemical aerosol properties on warm cloud droplet activation, Atmos. Chem. Phys.,
841   6(9), 2593–2649, doi:10.5194/acp-6-2593-2006, 2006.

842   McNeill, V. F.: Aqueous organic chemistry in the atmosphere: Sources and chemical processing of organic
843   aerosols, Environ. Sci. Technol., 49(3), 1237–1244, doi:10.1021/es5043707, 2015.

844   Mei, F., Setyan, A., Zhang, Q. and Wang, J.: CCN activity of organic aerosols observed downwind of urban
845   emissions during CARES, Atmos. Chem. Phys., 13(24), 12155–12169, doi:10.5194/acp-13-12155-2013, 2013.

846   Ng, N. L., Herndon, S. C., Trimborn, A., Canagaratna, M. R., Croteau, P. L., Onasch, T. B., Sueper, D., Worsnop,
847   D. R., Zhang, Q., Sun, Y. L. and Jayne, J. T.: An Aerosol Chemical Speciation Monitor (ACSM) for routine
848   monitoring of the composition and mass concentrations of ambient aerosol, Aerosol Sci. Technol., 45(7), 780–
849   794, doi:10.1080/02786826.2011.560211, 2011.

850   Ogawa, S., Setoguchi, Y., Kawana, K., Nakayama, T., Ikeda, Y., Sawada, Y., Matsumi, Y. and Mochida, M.:
851   Hygroscopicity of aerosol particles and CCN activity of nearly hydrophobic particles in the urban atmosphere
852   over Japan during summer, J. Geophys. Res., 121(12), 7215–7234, doi:10.1002/2015JD024636, 2016.

853   Petit, J. E., Favez, O., Albinet, A. and Canonaco, F.: A user-friendly tool for comprehensive evaluation of the
854   geographical origins of atmospheric pollution: Wind and trajectory analyses, Environ. Model. Softw., 88, 183–
855   187, doi:10.1016/j.envsoft.2016.11.022, 2017.

856   Petters, M. D. and Kreidenweis, S. M.: A single parameter representation of hygroscopic growth and cloud
857   condensation nucleus activity, Atmos. Chem. Phys. Atmos. Chem. Phys., 7, 1961–1971, doi:10.5194/acp-7-1961-
858   2007, 2007.

859   Prakash, J., Lohia, T., Mandariya, A. K., Habib, G., Gupta, T. and Gupta, S. K.: Chemical characterization and
860   quantitativ e assessment of source-specific health risk of trace metals in PM1.0 at a road site of Delhi, India,
861   Environ. Sci. Pollut. Res., 25(9), 8747–8764, doi:10.1007/s11356-017-1174-9, 2018.

862   Pringle, K. J., Tost, H., Pozzer, A., Pöschl, U. and Lelieveld, J.: Global distribution of the effective aerosol
863   hygroscopicity parameter for CCN activation, Atmos. Chem. Phys., 10(12), 5241–5255, doi:10.5194/acp-10-
864   5241-2010, 2010.

865   Rai, P., Furger, M., El Haddad, I., Kumar, V., Wang, L., Singh, A., Dixit, K., Bhattu, D., Petit, J.-E., Ganguly, D.,
866   Rastogi, N., Baltensperger, U., Tripathi, S. N., Slowik, J. G. and Prévôt, A. S. H.: Real-time measurement and
867   source apportionment of elements in Delhi's atmosphere, Sci. Total Environ., 742, 140332,
868   doi:10.1016/j.scitotenv.2020.140332, 2020.

869   Randall, D A; Wood, R A; Bony, S; Colman, R; Fichefet, T; Fyfe, J; Kattsov, V; Pitman, A; Shukla, J; Srinivasan,
870   J; Stouffer, R J; Sumi, A; Taylor, K. E.: Climate Models and Their Application, Clim. Chang. 2007 Phys. Sci.
871   Basis. Contrib. Work. Gr. I to Fourth Assess. Rep. Intergov. Panel Clim. Chang. Ed. by S. Solomon al., Cambridge
872   Univ. Press. Cambridge, U. K., New York., Chapter 8(United Kingdom: N. p., p.2007. Web.), 590–662,
873   doi:http://www.ipcc.ch/pdf/assessment-report/ar4/wg1/ar4-wg1-chapter8.pdf, 2007.

874   Richard, A., Gianini, M. F. D., Mohr, C., Furger, M., Bukowiecki, N. and Minguill, M. C.: and Physics Source
875   apportionment of size and time resolved trace elements and organic aerosols from an urban courtyard site in
876   Switzerland, , 8945–8963, doi:10.5194/acp-11-8945-2011, 2011.

877   Seinfeld, J. H. and Pandis, S. N.: Atmospheric cemistry and physics: From air pollution to climate change, Second
878   edi., John Wiley & Sons, Inc., 2006.

879   Shukla, A. K., Lalchandani, V., Bhattu, D., Dave, J. S., Rai, P., Thamban, N. M., Mishra, S., Gaddamidi, S.,
880   Tripathi, N., Vats, P., Rastogi, N., Sahu, L., Ganguly, D., Kumar, M., Singh, V., Gargava, P. and Tripathi, S. N.:
881   Real-time quantification and source apportionment of fine particulate matter including organics and elements in
882   Delhi during summertime, Atmos. Environ., 261, 118598, doi:10.1016/J.ATMOSENV.2021.118598, 2021.

883   Sjogren, S., Gysel, M., Weingartner, E., Baltensperger, U., Cubison, M. J. and Coe, H.: Hygroscopic growth and
884   water uptake kinetics of two-phase aerosol particles consisting of ammonium sulfate , adipic and humic acid
885   mixtures, , 38, 157–171, doi:10.1016/j.jaerosci.2006.11.005, 2007.

886   Sjogren, S., Gysel, M., Weingartner, E., Alfarra, M. R., Duplissy, J., Cozic, J., Crosier, J. and Coe, and U. B.:
887   Hygroscopicity of the submicrometer aerosol at the high-alpine site Jungfraujoch, 3580m a.s.l., Switzerland, ,
888   7231–7249, doi:10.5194/acp-12-7231-2012, 2012.

889   Stokes, R. H. and Robinson, R. A.: Interactions in Aqueous Nonelectrolyte Solutions. I. Solute-Solvent Equilibria,
890   J. Phys. Chem., 70(7), 2126–2131, doi:10.1021/j100879a010, 1966.

891   Su, H., Rose, D., Cheng, Y. F., Gunthe, S. S., Massling, A., Stock, M., Wiedensohler, A., Andreae, M. O. and
892   Pöschl, U.: Hygroscopicity distribution concept for measurement data analysis and modeling of aerosol particle
893   mixing state with regard to hygroscopic growth and CCN activation, Atmos. Chem. Phys, 10, 7489–7503,
894   doi:10.5194/acp-10-7489-2010, 2010.

895   Sun, Y., Wang, Z., Fu, P., Jiang, Q., Yang, T., Li, J. and Ge, X.: The impact of relative humidity on aerosol
896   composition and evolution processes during wintertime in Beijing , China, Atmos. Environ., 77, 927–934,
897   doi:10.1016/j.atmosenv.2013.06.019, 2013.

898   Sun, Y., Du, W., Fu, P., Wang, Q., Li, J., Ge, X., Zhang, Q., Zhu, C., Ren, L., Xu, W., Zhao, J., Han, T., Worsnop,
899   D. R. and Wang, Z.: Primary and secondary aerosols in Beijing in winter: Sources, variations and processes,
900   Atmos. Chem. Phys., 16(13), 8309–8329, doi:10.5194/acp-16-8309-2016, 2016.

901   Swietlicki, E., Hansson, H. C., Hämeri, K., Svenningsson, B., Massling, A., Mcfiggans, G., Mcmurry, P. H.,
902   Petäjä, T., Tunved, P., Gysel, M., Topping, D., Weingartner, E., Baltensperger, U., Rissler, J., Wiedensohler, A.
903   and Kulmala, M.: Hygroscopic properties of submicrometer atmospheric aerosol particles measured with H-
904   TDMA instruments in various environments—a review, Tellus B Chem. Phys. Meteorol., 60(3), 432–469,
905   doi:10.1111/j.1600-0889.2008.00350.x, 2008.

906   Tang, I. N. and Munkelwitz, H. R.: Water activities, densities, and refractive indices of aqueous sulfates and
907   sodium nitrate droplets of atmospheric importance, J. Geophys. Res., 99(D9), 18801, doi:10.1029/94JD01345,
908   1994.

909   Tobler, A., Bhattu, D., Canonaco, F., Lalchandani, V., Shukla, A., Thamban, N. M., Mishra, S., Srivastava, A. K.,
910   Bisht, D. S., Tiwari, S., Singh, S., Močnik, G., Baltensperger, U., Tripathi, S. N., Slowik, J. G. and Prévôt, A. S.
911   H.: Chemical characterization of PM2.5 and source apportionment of organic aerosol in New Delhi, India, Sci.
912   Total Environ., 745, 140924, doi:10.1016/J.SCITOTENV.2020.140924, 2020.

913   Topping, D. O. and McFiggans, G.: Tight coupling of particle size, number and composition in atmospheric cloud
914   droplet activation, Atmos. Chem. Phys., 12(7), 3253–3260, doi:10.5194/acp-12-3253-2012, 2012.

915   Tritscher, T., Jurnyi, Z., Martin, M., Chirico, R., Gysel, M., Heringa, M. F., Decarlo, P. F., Sierau, B., Prévt, A.
916   S. H., Weingartner, E. and Baltensperger, U.: Changes of hygroscopicity and morphology during ageing of diesel
917   soot, Environ. Res. Lett., 6(3), doi:10.1088/1748-9326/6/3/034026, 2011.

918   Wang, X., Shen, X. J., Sun, J. Y., Zhang, X. Y., Wang, Y. Q., Zhang, Y. M., Wang, P., Xia, C., Qi, X. F. and
919   Zhong, J. T.: Size-resolved hygroscopic behavior of atmospheric aerosols during heavy aerosol pollution episodes
920   in Beijing in December 2016, , 194(September), 188–197, doi:10.1016/j.atmosenv.2018.09.041, 2018a.

921   Wang, Y., Wu, Z., Ma, N., Wu, Y., Zeng, L., Zhao, C. and Wiedensohler, A.: Statistical analysis and
922   parameterization of the hygroscopic growth of the sub-micrometer urban background aerosol in Beijing, Atmos.

923   Environ., 175(December 2017), 184–191, doi:10.1016/j.atmosenv.2017.12.003, 2018b.

924   Wester, P., Mishra, A., Mukherji, A., Shrestha, A. B. and Change, C.: The Hindu Kush Himalaya Assessment,
925   edited by P. Wester, A. Mishra, A. Mukherji, and A. B. Shrestha, Springer International Publishing, Cham., 2019.

926   Wu, Z. J., Poulain, L., Henning, S., Dieckmann, K., Birmili, W., Merkel, M., van Pinxteren, D., Spindler, G.,
927   Müller, K., Stratmann, F., Herrmann, H. and Wiedensohler, A.: Relating particle hygroscopicity and CCN activity
928   to chemical composition during the HCCT-2010 field campaign, Atmos. Chem. Phys., 13(16), 7983–7996,
929   doi:10.5194/acp-13-7983-2013, 2013a.

930   Wu, Z. J., Poulain, L., Henning, S., Dieckmann, K., Birmili, W., Merkel, M., Van Pinxteren, D., Spindler, G.,
931   Stratmann, F., Herrmann, H. and Wiedensohler, A.: Sciences ess Atmospheric Chemistry and Physics Climate of
932   the Past Geoscientific Instrumentation Methods and Data Systems Relating particle hygroscopicity and CCN
933   activity to chemical composition during the HCCT-2010 field campaign, Atmos. Chem. Phys, 13, 7983–7996,
934   doi:10.5194/acp-13-7983-2013, 2013b.

935   Wu, Z. J., Zheng, J., Shang, D. J., Du, Z. F., Wu, Y. S., Zeng, L. M., Wiedensohler, A. and Hu, M.: Particle
936   hygroscopicity and its link to chemical composition in the urban atmosphere of Beijing , China , during
937   summertime, , 1123–1138, doi:10.5194/acp-16-1123-2016, 2016.

938   Yeung, M. C., Lee, B. P., Li, Y. J. and Chan, C. K.: Simultaneous HTDMA and HR-ToF-AMS measurements at
939   the HKUST supersite in Hong Kong in 2011, J. Geophys. Res., 119(16), 9864–9883, doi:10.1002/2013JD021146,
940   2014.

941   Zhang, Q., Jimenez, J. L., Worsnop, D. R. and Canagaratna, M.: A Case Study of Urban Particle Acidity and Its
942   Influence on Secondary Organic Aerosol, Environ. Sci. Technol., 41(9), 3213–3219, doi:10.1021/es061812j,
943   2007.

944   Zhang, S. L., Ma, N., Kecorius, S., Wang, P. C., Hu, M., Wang, Z. B., Größ, J., Wu, Z. J. and Wiedensohler, A.:
945   Mixing state of atmospheric particles over the North China Plain, Atmos. Environ., 125, 152–164,
946   doi:10.1016/J.ATMOSENV.2015.10.053, 2016.

947   Zhang, Y., Tang, L., Yu, H., Wang, Z., Sun, Y., Qin, W., Chen, W., Chen, C., Ding, A., Wu, J., Ge, S. and Chen,
948   C.: Chemical composition , sources and evolution processes of aerosol at an urban site in Yangtze River Delta ,
949   China during wintertime, Atmos. Environ., 123, 339–349, doi:10.1016/j.atmosenv.2015.08.017, 2015.

950   Zhao, P., Du, X., Su, J., Ding, J. and Dong, Q.: Aerosol hygroscopicity based on size-resolved chemical
951   compositions in Beijing, Sci. Total Environ., 716, 137074, doi:10.1016/J.SCITOTENV.2020.137074, 2020.

952